The Astrophysical Journal, 912:21 (23pp), 2021 May 1 https://doi.org/10.3847/1538-4357/abe9b8

Late-time Radio and Millimeter Observations of Superluminous Supernovae and Long Gamma-Ray Bursts: Implications for Central Engines, Fast Radio Bursts, and Obscured Star Formation

T. Eftekhari[1], B. Margalit[2,16], C. M. B. Omand[3], E. Berger[1], P. K. Blanchard[4], P. Demorest[5], B. D. Metzger[6], K. Murase[7,8,9,10], M. Nicholl[11,12], V. A. Villar[1], P. K. G. Williams[1,13], K. D. Alexander[4,16], S. Chatterjee[14], D. L. Coppejans[4], J. M. Cordes[14], S. Gomez[1], G. Hosseinzadeh[1], B. Hsu[1], K. Kashiyama[3,15], R. Margutti[4], and Y. Yin[1]

[1] Center for Astrophysics | Harvard & Smithsonian, Cambridge, MA 02138, USA
[2] Astronomy Department and Theoretical Astrophysics Center, University of California, Berkeley, Berkeley, CA 94720, USA
[3] Department of Physics, School of Science, The University of Tokyo, Tokyo 113-0033, Japan
[4] Center for Interdisciplinary Exploration and Research in Astrophysics (CIERA) and Department of Physics and Astronomy, Northwestern University, 1800 Sherman Avenue, Evanston, IL 60201, USA
[5] National Radio Astronomy Observatory, Socorro, NM 87801, USA
[6] Department of Physics and Columbia Astrophysics Laboratory, Columbia University, New York, NY 10027, USA
[7] Department of Physics, The Pennsylvania State University, University Park, PA 16802, USA
[8] Department of Astronomy & Astrophysics, The Pennsylvania State University, University Park, PA 16802, USA
[9] Center for Multimessenger Astrophysics, The Pennsylvania State University, University Park, PA 16802, USA
[10] Yukawa Institute for Theoretical Physics, Kyoto University, Kyoto 606-8502, Japan
[11] Institute for Astronomy, University of Edinburgh, Royal Observatory, Blackford Hill, Edinburgh EH9 3HJ, UK
[12] Birmingham Institute for Gravitational Wave Astronomy and School of Physics and Astronomy, University of Birmingham, Birmingham B15 2TT, UK
[13] American Astronomical Society, Washington, DC 20006, USA
[14] Cornell Center for Astrophysics and Planetary Science and Department of Astronomy, Cornell University, Ithaca, NY 14853, USA
[15] Research Center for the Early Universe, The University of Tokyo, Tokyo 113-0033, Japan
Received 2020 October 13; revised 2021 February 20; accepted 2021 February 23; published 2021 April 30

Abstract

We present the largest and deepest late-time radio and millimeter survey to date of superluminous supernovae (SLSNe) and long-duration gamma-ray bursts (LGRBs) to search for associated nonthermal synchrotron emission. Using the Karl G. Jansky Very Large Array (VLA) and the Atacama Large Millimeter/submillimeter Array (ALMA), we observed 43 sources at 6 and 100 GHz on a timescale of $\sim$ 1–19 yr post-explosion. We do not detect radio/millimeter emission from any of the sources, with the exception of a 6 GHz detection of PTF10hgi, as well as the detection of 6 GHz emission near the location of the SLSN PTF12dam, which we associate with its host galaxy. We use our data to place constraints on central engine emission due to magnetar wind nebulae and off-axis relativistic jets. We also explore nonrelativistic emission from the SN ejecta, and place constraints on obscured star formation in the host galaxies. In addition, we conduct a search for fast radio bursts (FRBs) from some of the sources using VLA phased-array observations; no FRBs are detected to a limit of 16 mJy (7σ; 10 ms duration) in about 40 minutes on source per event. A comparison to theoretical models suggests that continued radio monitoring may lead to detections of persistent radio emission on timescales of $\gtrsim$ a decade.

Unified Astronomy Thesaurus concepts: Radio transient sources (2008); Extragalactic radio sources (508); Radio astrometry (1337); Core-collapse supernovae (304); Supernova remnants (1667); Relativistic jets (1390); Magnetars (992); Star formation (1569); Stellar physics (1621)

1. Introduction

The advent of wide-field untargeted optical surveys has led to the discovery of hydrogen-poor superluminous supernovae (SLSNe[17]), a rare class of core-collapse supernovae (SNe) with luminosities up to 100 times larger than ordinary SNe (e.g., Chomiuk et al. 2011; Quimby et al. 2011b; Gal-Yam 2012). The energy source of SLSNe has been a topic of debate, with ideas ranging from pair-instability explosions (Gal-Yam et al. 2009) to interaction with a dense hydrogen-poor circumstellar medium (Chevalier & Irwin 2011), and the spin-down of a millisecond magnetar central engine (Kasen & Bildsten 2010; Woosley 2010). In recent years, a growing line of evidence has emerged in favor of a central engine origin. Indeed, the light-curve evolution of these events can be well-characterized by the dipole spin-down of strongly magnetized neutron stars with initial spin periods of $\sim$ 1–10 ms and large magnetic fields of $\sim 10^{13}$–10^{15} G (Inserra et al. 2013; Nicholl et al. 2014, 2017c; Blanchard et al. 2020).

Some similarities have also been noted between SLSNe and long-duration gamma-ray bursts (LGRBs). Namely, both are rare explosions that arise from stripped massive stars, exhibit a preference for low metallicity host galaxies (e.g., Modjaz et al. 2008; Levesque et al. 2010; Lunnan et al. 2014), share ejecta properties as evidenced by nebular-phase spectra (Nicholl et al. 2016a; Jerkstrand et al. 2017; Nicholl et al. 2019), and appear to be powered by central engines (Mazzali et al. 2014; Margalit et al. 2018b); although in the case of

[16] NASA Einstein Fellow.
[17] For simplicity we refer to the hydrogen-poor (Type I) events as SLSNe. The hydrogen-rich events appear to simply be an extension of the SN IIn population.

LGRBs, black hole engines have also been assumed (e.g., MacFadyen & Woosley 1999; Metzger et al. 2011).

Another intriguing connection to SLSNe has been suggested by the discovery and localization of the repeating fast radio burst (FRB) FRB 121102 (Spitler et al. 2014, 2016) to a low metallicity star-forming galaxy (Chatterjee et al. 2017; Tendulkar et al. 2017) and an associated parsec-scale persistent radio source (Marcote et al. 2017), whose large and variable rotation measure (RM) indicates a highly magnetized and dynamic environment (Michilli et al. 2018). These properties have prompted theories suggesting that FRB production is associated with the birth of young, millisecond magnetars in SLSN and/or LGRB explosions (Murase et al. 2016; Piro 2016; Kashiyama & Murase 2017; Metzger et al. 2017; Nicholl et al. 2017c; Margalit et al. 2018a, 2018b).

More recently, the localizations of 10 apparently non-repeating FRBs (Bannister et al. 2019; Prochaska et al. 2019; Ravi et al. 2019; Bhandari et al. 2020; Heintz et al. 2020; Law et al. 2020; Macquart et al. 2020) to more massive galaxies suggest that some FRBs may be produced by magnetars formed from an older progenitor population such as binary neutron star mergers or accretion-induced collapse (AIC) of white dwarfs (Margalit et al. 2019). Indeed, the recent discovery of a luminous, millisecond-duration radio burst from the Galactic magnetar SGR 1935+2154 (Scholz & Chime/Frb Collaboration 2020; Bochenek et al. 2020) may support a connection between magnetars and FRBs (Margalit et al. 2020). Finally, two additional repeating FRBs (FRBs 180916 and 190711) have been localized to host galaxies (Heintz et al. 2020; Marcote et al. 2020). Similar to the host of FRB 121102, the host galaxies of these events are both less luminous and less massive than the host galaxies of the apparently non-repeating FRBs, though they exhibit a range of star formation rates (SFRs; Heintz et al. 2020).

The long-term radio and millimeter properties of SLSNe, which may shed light on their energy source and probe a connection with FRB 121102–like systems, have not been explored to date. Early radio follow-up (timescales of $\lesssim 1-8$ yr) has yielded only nondetections (e.g., Coppejans et al. 2018; Hatsukade et al. 2018). On the other hand, follow-up of the SLSN PTF10hgi on a timescale of about 8–10 yr post-explosion has led to a number of radio detections (Eftekhari et al. 2019; Law et al. 2019; Mondal et al. 2020). While a magnetar origin has not yet been confirmed for this source, the available data are consistent with emission powered by a central engine, either from a magnetar-powered nebula or an off-axis jet (Eftekhari et al. 2019).

In addition to searches for radio nebulae from putative central engines, radio and millimeter observations provide insight into the properties of non- or mildly relativistic ejecta (e.g., Berger et al. 2002), as well as obscured star formation in the host galaxies of these events (e.g., Berger et al. 2003; Hatsukade et al. 2018; Greiner et al. 2016).

Here we present deep late-time radio and millimeter observations of 43 SLSNe and LGRBs to search for nonthermal synchrotron emission from these sources, which may shed light on their central engines, connection to FRBs, slow ejecta, and host galaxies. Our study provides the largest and deepest sample of radio and millimeter observations of SLSNe to date. We use the data to explore magnetar wind nebulae, off-axis jets, emission from the nonrelativistic SN ejecta, and obscured star formation in the host galaxies. The paper is structured as follows. We present our observations in Section 2. Constraints on obscured star formation in the host galaxies are presented in Section 3. In Sections 4.1 and 4.2, we examine synchrotron emission due to nonrelativistic and relativistic outflows, respectively. We place constraints on putative magnetar wind nebulae in Section 5, and we summarize our results in Section 6. Throughout the paper, we use the latest Planck cosmological parameters, $H_0 = 67.8\ \mathrm{km\ s^{-1}\ Mpc^{-1}}$, $\Omega_m = 0.308$, and $\Omega_\Lambda = 0.692$ (Planck Collaboration et al. 2016).

2. VLA and ALMA Observations

2.1. Sample Selection

The SLSNe observed with the Karl G. Jansky Very Large Array (VLA) represent a complete (as of 2017 February) volume-limited sample to a distance twice that of FRB 121102 ($z \lesssim 0.35$), and with a timescale of $\gtrsim 5$ yr post-explosion, leading to 15 SLSNe. Of these, three events were previously observed in the radio at early time, leading to nondetections: PTF09cnd (Chandra et al. 2009, 2010), SN2012il (Chomiuk et al. 2012), and SN2015bn (Nicholl et al. 2016b, 2018); see Table 1. Observations of PTF10hgi obtained as part of this work were presented in Eftekhari et al. (2019). We also observed seven LGRBs with the VLA, of which two were detected at early times: (i) GRB 020903 had a 5 GHz flux density of $\approx 100\ \mu$Jy at 0.5 yr post-explosion, declining as $F \propto t^{-1.1}$ (Soderberg et al. 2004); and (ii) GRB 030329 was last detected 4.9 yr post-explosion with a 5 GHz flux density of 70 μJy and a decline rate of $t^{-1.3}$ (Mesler et al. 2012). The contribution from an afterglow at the time of our observations ($\delta t \approx 5490$ and $\delta t \approx 5323$ days for GRB 020903 and GRB 030329, respectively) is expected to be negligible.

We additionally observed 29 SLSNe with the Atacama Large Millimeter/submillimeter Array (ALMA), seven of which overlap with our VLA sample. These events were observed as part of two observing campaigns. Events observed during the first campaign (2017.1.00280.S; PI: Berger) constitute all sources accessible to ALMA (as of March 2017)[18] with a timescale of $\gtrsim 3$ yr post-explosion and a distance of $z \lesssim 0.5$. The second campaign (2019.1.01663.S; PI: Eftekhari) consists of all events with decl. $< 30°$ and $z < 0.4$, with the exception of SN2017egm, which has been observed as part of a dedicated ALMA campaign; the source is also observed at early times in the radio (Bright et al. 2017; Bose et al. 2018; Coppejans et al. 2018).

2.2. VLA Continuum Observations

We obtained 6 GHz (C-band) radio observations of our sample with the VLA in configurations A and B with a total on-source integration time of ≈ 40 minutes per target. The details of the observations are summarized in Table 2. All observations obtained in 2017 utilized the 8 bit samplers with ~ 2 GHz bandwidth (excluding excision of edge channels and radio frequency interference (RFI)), while our 2019 observations were configured using the 3 bit samplers, providing the full 4 GHz of bandwidth across the observing band.

[18] The sole exception is PS1-14bj, which was not observed due to a scheduling error.

Table 1
Existing Radio Observations of SLSNe from the Literature

Source	z	Explosion Date (MJD)	δt[a] (days)	Frequency (GHz)	Flux (μJy)	Reference
SN2005ap	0.2832	53424	3009	1.5	< 75	Schulze et al. (2018)
…	…	…	3613, 3668[l]	3	< 30	Law et al. (2019)
SN2006oz	0.376	54025	2915, 2979[l]	3	< 24	Law et al. (2019)
SN2007bi	0.1279	54075	3546, 3593[l]	3	< 66	Law et al. (2019)
SN2009jh	0.35	55014	2256, 2309[l]	3	< 18	Law et al. (2019)
PTF09atu	0.5015	55025[b]	2011, 2068[l]	3	< 24	Law et al. (2019)
PTF09cnd	0.258	55006	85	8.46	< 90	Chandra et al. (2009)
…	…	…	85	4.86	< 96	Chandra et al. (2009)
…	…	…	85	1.41	< 579	Chandra et al. (2009)
…	…	…	140	8.46	< 69	Chandra et al. (2010)
…	…	…	142	4.86	< 147	Chandra et al. (2010)
…	…	…	147	1.41	< 600	Chandra et al. (2010)
…	…	…	2416, 2483[l]	3	< 33	Law et al. (2019)
PS1-10awh	0.908	55467	39	4.9	< 45	Chomiuk et al. (2011)
PS1-10bzj	0.65	55523[c]	48	4.96	< 87	Coppejans et al. (2018)
PS1-10ky	0.956	55299[d]	156	4.9	< 51	Chomiuk et al. (2011)
PTF10aagc	0.206	55439[e]	2041	3	< 15.6	Hatsukade et al. (2018)
PTF10hgi	0.0987	55322[f]	2524	6	47.3	Eftekhari et al. (2019)
…	…	…	2469, 2547[l]	3	47	Law et al. (2019)
…	…	…	3220, 3250[l]	0.6	< 36	Mondal et al. (2020)
…	…	…	3207	1.2	64	Mondal et al. (2020)
…	…	…	3289	3.3	66	Mondal et al. (2020)
…	…	…	3263	6	46	Mondal et al. (2020)
…	…	…	3308	15	47	Mondal et al. (2020)
PTF10uhf	0.288	55388[g]	1951	3	< 80.9[k]	Hatsukade et al. (2018)
SN2010gx	0.230	55251	2154	3	< 20.7	Hatsukade et al. (2018)
…	…	…	2295, 2339[l]	3	< 33	Law et al. (2019)
SN2010kd	0.1	55499	2341, 2390[l]	3	< 42	Law et al. (2019)
SN2011kg	0.192	55912	1678	3	< 22	Hatsukade et al. (2018)
SN2011ke	0.14	55651	2113, 2175[l]	3	< 36	Law et al. (2019)
SN2012il	0.175	55919	44	5.9	< 21	Chomiuk et al. (2012)
PTF12dam	0.107	56022	1697	3	< 141.5[k]	Hatsukade et al. (2018)
iPTF15cyk	0.539	57249[h]	61	5.4	< 30	Kasliwal et al. (2016)
…	…	…	94	5.4	< 23	Kasliwal et al. (2016)
…	…	…	124	5.4	< 23	Kasliwal et al. (2016)
SN2015bn	0.1136	57013	318	7.4	< 75	Nicholl et al. (2016a)
…	…	…	318	22	< 40	Nicholl et al. (2016a)
…	…	…	867	21.8	< 48	Nicholl et al. (2018)
…	…	…	867	33.5	< 63	Nicholl et al. (2018)
Gaia16apd	0.1013	57512[i]	26	5.9	< 20.4	Coppejans et al. (2018)
…	…	…	26	21.8	< 45.9	Coppejans et al. (2018)
…	…	…	203	5.9	< 15.3	Coppejans et al. (2018)
…	…	…	203	21.8	< 30.1	Coppejans et al. (2018)
SN2017egm	0.0307	57887[j]	34	15.5	< 1800[k]	Bright et al. (2017)
…	…	…	38	5	< 60	Bright et al. (2017)
…	…	…	39	10	< 76.8	Bose et al. (2018)
…	…	…	39	1.6	< 96	Bose et al. (2018)
…	…	…	46	33	< 150	Coppejans et al. (2018)
…	…	…	47	10	< 86.1	Bose et al. (2018)
…	…	…	74	33	< 33.6	Coppejans et al. (2018)

Notes. Limits correspond to 3σ.
[a] Explosion rest frame.
[b] De Cia et al. (2018)..
[c] Assuming a fast rise rest-frame time of 25 days and a peak time of MJD 55,563.65±2 (Lunnan et al. 2018).
[d] Assuming a rest-frame rise time of 50 days and a peak time of MJD 55,397 (Chomiuk et al. 2011).
[e] Assuming a rest-frame rise time of 50 days and a peak time of MJD 55,499.5 (Quimby et al. 2018).
[f] Inserra et al. (2013).
[g] Assuming a rest-frame rise time of 50 days and a peak time of MJD 55,452.3 (Quimby et al. 2018).
[h] We assume a peak time of MJD 57,293.5 and a rest-frame rise time of 60 days as in Coppejans et al. (2018).
[i] From Yan et al. (2015), the peak time is MJD 57,541 and the rest-frame rise time is 29 days (Nicholl et al. 2017b).
[j] Nicholl et al. (2017a).
[k] The host galaxy contribution to the flux density is unknown, so we adopt their detection value as an upper limit.
[l] 3σ limit averaged over two epochs.

We processed the data within the Common Astronomy Software Application (CASA) software package (McMullin et al. 2007). We performed bandpass and flux density calibration using 3C286 and 3C48. Complex gain calibrators for individual sources are listed in Table 2. We imaged each field using 2048×2048 pixels at a scale of $0.07 - 0.2$ arcsec

Table 2
Karl G. Jansky Very Large Array Radio Observations at 6 GHz

Source	R.A. (J200)	Decl. (J200)	Observation Date	Bandpass Calibrator	Phase Calibrator	$t_{\rm int}$ (minutes)	Beam Size (arcsec)	Beam Angle (deg)	rms (μJy)
SN1999as	09:16:30.86	+13:39:02.2	2017 Sep 16	3C48	J0854+2006	37.80	1.30 × 1.03	−59.42	6.67
SN2005ap	13:01:14.84	+27:43:31.4	2017 Nov 26	3C286	J1310+3220	19.75	0.96 × 0.95	−66.36	11.39
…	…	…	2019 Sep 03	3C286	J1310+3220	45.63	0.33 × 0.30	83.64	4.69
SN2006oz	22:08:53.56	+00:53:50.4	2017 Sep 14	3C48	J2212+0152	37.55	1.17 × 0.92	11.13	6.74
SN2007bi	13:19:20.19	+08:55:44.3	2017 Nov 26	3C286	J1309+1154	19.75	1.18 × 1.04	85.43	12.14
SN2009jh	14:49:10.08	+29:25:11.4	2017 Dec 15	3C286	J1443+2501	43.15	0.89 × 0.86	22.65	6.50
PTF09cnd	16:12:08.94	+51:29:16.1	2017 Dec 15	3C286	J1549+5038	42.15	0.94 × 0.75	22.25	6.18
SN2010kd	12:08:01.11	+49:13:31.1	2017 Oct 26	3C286	J1219+4829	37.55	1.09 × 0.88	76.33	4.78
SN2010gx	11:25:46.71	−08:49:41.4	2017 Oct 26	3C286	J1131−0500	38.55	1.88 × 0.90	−42.57	5.64
SN2011ke	13:50:57.77	+26:16:42.8	2017 Dec 02	3C286	J1407+2827	41.15	1.05 × 0.90	−54.68	4.97
SN2011kf	14:36:57.53	+16:30:56.6	2017 Dec 02	3C286	J1446+1721	41.10	1.09 × 0.90	−45.20	5.56
…	…	…	2019 Sep 03	3C286	J1446+1721	44.27	0.33 × 0.30	37.63	4.62
SN2011kg	01:39:45.51	+29:55:27.0	2017 Sep 15	3C48	J0151+2744	40.80	1.36 × 0.96	−79.72	6.30
SN2012il	09:46:12.91	+19:50:28.7	2017 Sep 16	3C48	J0954+1743	40.5	1.12 × 0.99	−50.17	5.33
…	…	…	2019 Aug 27	3C286	J0954+1743	45.60	0.31 × 0.27	−1.32	5.32
PTF12dam	14:24:46.20	+46:13:48.3	2017 Dec 15	3C286	J1417+4607	43.15	0.95 × 0.74	17.84	8.47
…	…	…	2019 Sep 03	3C286	J1417+4607	45.63	0.39 × 0.28	−63.41	10.04
LSQ12dlf	01:50:29.80	−21:48:45.4	2017 Sep 15	3C48	J0135−2008	40.80	1.15 × 1.04	−32.01	8.96
GRB020903	22:48:42.34	−20:46:09.3	2017 Sep 14	3C48	J2243−2544	39.45	1.89 × 0.91	13.70	6.60
GRB030329	10:44:50.03	+21:31:18.15	2017 Oct 24	3C48	J1051+2119	40.50	1.48 × 1.04	−70.47	5.60
GRB050826	05:51:01.59	−02:38:35.4	2017 Sep 16	3C48	J0541−0541	40.50	1.16 × 0.92	0.96	6.46
GRB061021	09:40:36.12	−21:57:05.4	2017 Oct 24	3C48	J0927−2034	40.50	2.15 × 0.88	−22.66	5.75
GRB090417B	13:58:44.80	+47:00:55.0	2017 Dec 02	3C286	J1417+4607	41.20	0.96 × 0.89	−25.99	5.67
GRB111225A	00:52:37.22	+51:34:19.5	2017 Sep 15	3C48	J0105+4819	40.85	1.41 × 0.87	84.14	6.00
GRB120422A	09:07:38.38	+14:01:07.5	2017 Oct 24	3C48	J0854+2006	38.80	1.30 × 1.05	−62.28	5.07

per pixel using multifrequency synthesis (MFS; Sault & Wieringa 1994) and *w*-projection with 128 planes (Cornwell et al. 2008). Flux densities at the source positions (and image rms values) were extracted using the `imtool` program as part of the `pwkit`[19] package (Williams et al. 2017) (Table 2).

In addition to the detection of PTF10hgi, with $F_\nu = 47 \pm 7$ μJy, reported in Eftekhari et al. (2019), we detect radio emission near the location of the SLSN PTF12dam with a flux density $F_\nu = 117 \pm 12$ μJy; see Figure 1. This is comparable to the 3 GHz detection presented in Hatsukade et al. (2018) with $F_\nu = 141.5 \pm 5.1$ μJy. The radio emission is offset from the SN position by ∼1 arcsecond and is instead centered on, and traces, the optical emission from the host galaxy. Thus the emission is most likely related to star formation in the host galaxy (see discussion in Section 3). Indeed, the emission is resolved out in our second-epoch, A-configuration observation with a decreased flux density $F_\nu = 61.5 \pm 10.8$ μJy, indicative of an extended source. No clear radio emission (signal-to-noise ratio, S/N$> 5\sigma$) is detected from the remainder of the SLSNe in our sample, or from the location of any of the LGRBs in our sample, with typical rms values of 5–10 μJy.

We report marginal detections near the positions of SN2009jh and GRB 050826. In the case of SN2009jh, the source significance is 3.6σ ($F_\nu = 23.3 \pm 6.4$ μJy) but with an offset of $1\farcs6 \pm 0\farcs3$ from the SN position, and we therefore consider it unlikely to be related to the SN. Similarly, for GRB 050826, the source significance is only 2.5σ ($F_\nu = 23 \pm 9$ μJy) with an offset of $1\farcs0 \pm 0\farcs5$ from the GRB position.

[19] Available at https://github.com/pkgw/pwkit.

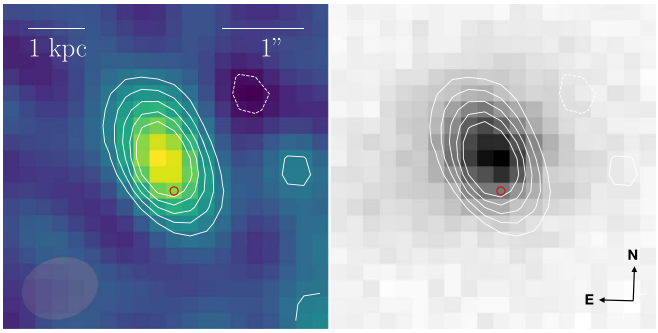

Figure 1. Left: radio continuum image of the host galaxy of PTF12dam from our VLA 6 GHz (C-band) observation in B-configuration. Contours correspond to −2, 2, 3, 4, 5, and 6 times the rms noise of the image. The synthesized beam (0.95"× 0.74") is shown in the lower left corner. Shown as a red circle is the optical position of the SN. Right: Pan-STARRS optical *i*-band image of the host galaxy with radio contours overlaid.

2.3. Phased VLA Observations

In addition to standard continuum observations, we also obtained phased-array observations with the VLA to search for FRBs from the observed sources. Similar searches for FRBs from the locations of SLSNe and LGRBs were presented in Law et al. (2019) and Hilmarsson et al. (2020), yielding no detections. We present here the results of our initial VLA sample of events observed in 2017. The phased-array data were recorded with 256 μs time resolution and 2 MHz channels with 2 GHz total bandwidth. Each raw filterbank file is divided into a channelized time series with 1 GHz bandwidth centered at 5 and 7 GHz. We performed a standard RFI search using the `rfifind` routine in `PRESTO` (Ransom 2001) with 2 s integration times. The RFI-excised maps are applied to the data

Table 3
ALMA Millimeter Observations at 100 GHz

Source	R.A. (J200)	Decl. (J200)	Observation Date	Bandpass Calibrator	Phase Calibrator	$t_{\rm int}$ (minutes)	Beam Size (arcsec)	Beam Angle (deg)	rms (μJy)
SN2006oz	22:08:53.56	+00:53:50.4	2017 Dec 17	J2148+0657	J2156-0037	21.67	0.41 × 0.31	−85.96	17.61
SN2007bi	13:19:20.19	+08:55:44.3	2018 Mar 18	J1229+0203	J1254+1141	22.68	1.19 × 1.153	−57.23	17.70
PTF10hgi	16:37:47.00	+06:12:32.3	2018 Jan 11	J1550+0527	J1658+0741	22.18	0.48 × 0.37	73.44	14.66
SN2010gx	11:25:46.71	−08:49:41.4	2018 Jan 12	J1058+0133	J1135−0428	21.17	0.53 × 0.39	61.30	19.04
SN2011kf	14:36:57.53	+16:30:56.6	2018 Jan 28	J1550+0527	J1446+1721	23.69	0.72 × 0.63	5.17	16.70
SN2012il	09:46:12.91	+19:50:28.7	2017 Dec 15	J0854+2006	J0940+2603	26.21	0.48 × 0.37	70.72	19.07
LSQ12dlf	01:50:29.80	−21:48:45.4	2017 Dec 30	J0006−0623	J0151−1732	20.66	0.40 × 0.29	−76.78	17.06
SSS120810	23:18:01.80	−56:09:25.6	2017 Dec 17	J2357−5311	J2336−5236	22.68	0.38 × 0.36	−12.61	17.29
SN2013dg	13:18:41.35	−07:04:43.0	2018 Jan 13	J1256−0547	J1312−0424	21.17	0.67 × 0.58	80.41	20.63
LSQ14bdq	10:01:41.60	−12:22:13.4	2017 Dec 20	J1037-2934	J0957−1350	21.17	0.46 × 0.32	71.07	18.50
LSQ14mo	10:22:41.53	−16:55:14.4	2017 Dec 20	J1037−2934	J0957−1350	20.66	0.47 × 0.32	72.08	20.22
LSQ14an	12:53:47.83	−29:31:27.2	2017 Dec 04	J1337-1257	J1305−2850	20.66	0.25 × 0.21	87.49	16.11
LSQ14fxj	02:39:12.61	+03:19:29.6	2017 Dec 29	J0239+0416	J0239+0416	22.18	0.42 × 0.30	−76.52	22.18
CSS140925	00:58:54.11	+18:13:22.2	2018 Jan 01	J0238+1636	J0117+1418	25.71	0.54 × 0.32	−52.06	16.68
SN2015bn	11:33:41.57	+00:43:32.2	2018 Jan 12	J1058+0133	J1135−0428	21.67	0.57 × 0.39	55.43	18.22
OGLE15sd	01:42:21.46	−71:47:15.6	2017 Dec 28	J2357−5311	J0112−6634	53.42	0.45 × 0.36	−22.87	12.08
SN2016ard	14:10:44.55	−10:09:35.4	2018 Jan 25	J1337−1257	J1406−0848	21.17	0.82 × 0.58	−86.36	16.93
iPTF16bad	17:16:40	+22:04:52.47	2019 Dec 12	J1924−2914	J1722+2815	69.55	3.58 × 2.77	−6.69	14.06
SN2016els	20:30:13.92	−10:57:01.81	2019 Oct 20	J1924−2914	J2025−0735	18.44	1.49 × 0.95	87.45	20.16
SN2017gci	06:46:45.026	−27:14:55.86	2019 Dec 14	J0538−4405	J0632−2614	18.14	2.70 × 2.28	88.54	15.39
SN2017jan	03:07:22.570	−64:23:01.00	2019 Dec 25	J0334−4008	J0303−6211	21.17	3.31 × 2.68	−42.71	21.46
SN2018bsz	16:09:39.1	−32:03:45.73	2019 Dec 17	J1517−2422	J1556−3302	18.14	3.09 × 2.16	−81.01	15.09
SN2018ffj	02:30:59.77	−17:20:26.82	2019 Dec 23	J0006−0623	J0212−1746	18.14	3.31 × 2.34	−89.71	17.81
SN2018ffs	20:54:37.16	+22:04:51.47	2019 Nov 11	J2253+1608	J2051+1743	29.23	1.96 × 1.66	−8.35	17.99
SN2018gft	23:57:17.95	−15:37:53.27	2019 Dec 13	J0006−0623	J2354−1513	18.14	2.83 × 2.24	78.35	17.15
SN2018hti	03:40:53.750	+11:46:37.29	2019 Dec 26	J0423−0120	J0334+0800	20.16	2.89 × 2.66	−41.55	17.27
SN2018ibb	04:38:56.960	−20:39:44.01	2019 Dec 24	J0423−0120	J0416−1851	18.14	3.03 × 2.39	−71.73	19.19
SN2018jfo	11:23:38.618	+25:59:51.95	2019 Dec 31	J1256−0547	J1148+1840	44.86	3.82 × 2.39	−36.95	17.93
SN2018lfe	09:33:29.556	+00:03:08.39	2019 Dec 30	J0750+1231	J0930+0034	18.65	3.55 × 2.52	73.94	20.68

for subsequent processing. For each source, we incoherently dedispersed the data at 1000 trial dispersion measures (DMs) ranging up to DM = 5000 pc cm^{-3} with a step size of 5, corresponding to a maximum redshift $z \sim 7$, well beyond the max redshift of our sample ($z \sim 0.57$), and indeed well above the maximum observed DM for any FRB observed to date.[20] This additionally allows for a substantial host galaxy DM contribution. Following dedispersion, we normalize the time series by performing a standard red noise removal. Individual scans are then searched for FRBs using the matched-filtering algorithm `single_pulse_search.py` (Ransom 2001).

Following the prescription of Cordes & McLaughlin (2003), the minimum detectable flux density for an FRB is given by:

$$S_{\rm min} = \frac{({\rm S/N})_{\rm min}\,{\rm SEFD}}{\sqrt{n_{\rm pol}\Delta\nu W}} \quad (1)$$

where $n_{\rm pol}$ is the number of summed polarizations, $\Delta\nu$ is the bandwidth, W is the intrinsic pulse width, $({\rm S/N})_{\rm min}$ is the minimum signal-to-noise threshold, and SEFD refers to the system equivalent flux density. Assuming a phasing efficiency factor of 0.9 and a nominal 10 ms pulse width, we find a minimum detectable flux density of $S_{\rm min} \approx 16$ mJy (7σ) for our observations.

We do not detect any FRBs from our sample. We place limits on the maximum energy of an FRB emitted from each source following the prescription of Cordes & Chatterjee (2019), in which the burst energy is given by:

$$E_{\rm b,max} = 4\pi S_\nu W \Delta\nu d_L f_b\,, \quad (2)$$

where we assume a beaming fraction $f_b = 0.5$. For the range of redshifts probed by our initial VLA sample of SLSNe ($z \sim 0.101 - 0.376$), we find $E_{\rm b,max} \lesssim 2 \times 10^{37}$–$4 \times 10^{38}$ erg. This is comparable to the range of inferred burst energies for the lowest-energy bursts from FRB 121102, with $E_b \sim 10^{37}$–10^{38} erg (Gourdji et al. 2019). Thus, while we are sensitive to the low-energy range of FRBs (from FRB 121102), given the intermittent nature of FRB 121102, the short duration of our observations (≈40 min per source) is prohibitively small. A significant time investment with the Green Bank Telescope (GBT), Arecibo, or the Five-hundred-meter Aperture Spherical Telescope (FAST) may reveal bursts from these sources.

2.4. ALMA Observations

We obtained millimeter observations with ALMA in Band 3 (∼100 GHz) of 28 SLSNe. Flux density and complex gain calibrators are listed in Table 3. In all cases, we use the ALMA data products, which utilize standard imaging techniques within CASA. Each field is imaged using MFS, Briggs weighting with a robust parameter of 0.5, and a standard gridding convolution function. Image scales span $0.04 - 0.2$ arcseconds per pixel, with typical image sizes of about 1500×1500 pixels. Flux densities and image rms values were

[20] http://frbcat.org/

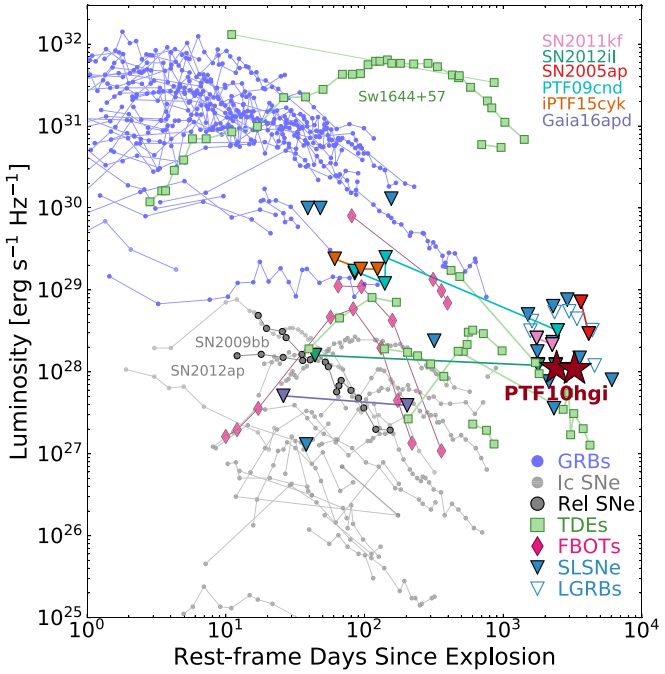

Figure 2. Radio luminosities at 6 GHz for our sample of SLSNe (blue filled triangles) and LGRBs (blue open triangles), compared to the 6–10 GHz luminosities of other classes of radio transients, including relativistic SNe (Soderberg et al. 2010; Margutti et al. 2014), "normal" hydrogen-poor core-collapse Ibc SNe (Soderberg et al. 2005, 2006; Chomiuk et al. 2012), fast blue optical transients (Margutti et al. 2019; Coppejans et al. 2020; Ho et al. 2019, 2020; D. L. Coppejans et al. 2021, in preparation), GRBs (Chandra & Frail 2012), and TDEs (Zauderer et al. 2011; Berger et al. 2012; Cenko et al. 2012; Zauderer et al. 2013; Irwin et al. 2015; Alexander et al. 2017b; Brown et al. 2017; Saxton et al. 2017; Eftekhari et al. 2018; Mattila et al. 2018). We highlight SLSNe with multiple epochs of observations from the literature (references are given in Table 1).

obtained using the `imtool` program as part of the `pwkit` package.

We do not detect millimeter emission from any of our sources with the exception of a 3σ detection near the location of SN2007bi, with a flux density $F_\nu = 55.3 \pm 18.8$ μJy (R.A. $= 13^{\rm h}19^{\rm m}20\overset{\rm s}{.}226$, decl. $= +08^\circ55'43\overset{''}{.}85$; J2000). To compare the position of the millimeter source relative to the SN position, we use archival images of SN2007bi from the Liverpool Telescope (Young et al. 2010), which are first matched to an absolute astrometric system. We find that the millimeter source is offset from the SN position by $1\overset{''}{.}0 \pm 0\overset{''}{.}6$ and is thus unlikely to be related to the SN. We similarly compare the position of this source to that of the host galaxy of SN2007bi using a wide-field i-band image from the Panoramic Survey Telescope and Rapid Response System (Pan-STARRS1) 3π survey. We first perform relative astrometry between the PS1/3π image and the Liverpool image and find an astrometric tie uncertainty of $\sigma_{\rm host} \approx 0\overset{''}{.}6$. Comparing the position of the millimeter source to this image, we find that the source is offset from the host galaxy position by $1\overset{''}{.}5 \pm 0\overset{''}{.}6$. We thus conclude that the weak ALMA detection is unlikely to be related to the SN or the host galaxy.

2.5. Comparison to Other Transients

In Figure 2 we plot the 6 GHz radio luminosity upper limits of our sample of SLSNe and LGRBs, compared to the 6–10 GHz light curves of other classes of transients, including relativistic SNe, normal SNe Ib/c, fast blue optical transients, and tidal disruption events (TDEs). We also include observations of LGRBs and SLSNe from the literature.

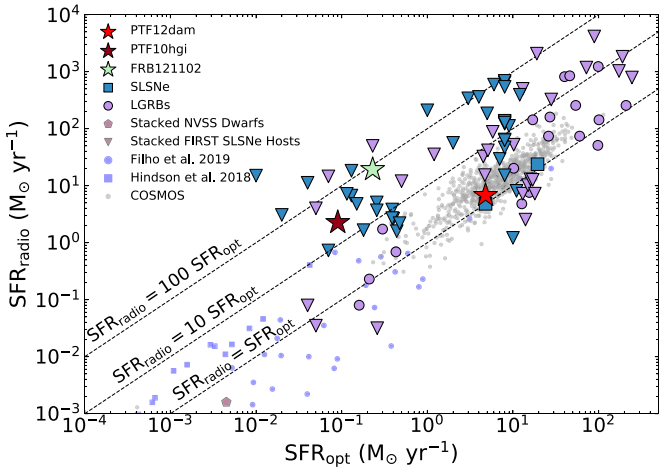

Figure 3. Radio vs. optical SFRs for SLSNe (blue) and LGRBs (purple). Triangles correspond to 3σ upper limits. Also shown are our detections for PTF10hgi (Eftekhari et al. 2019) and PTF12dam, as well as FRB 121102 (assuming a star formation origin for the radio emission). We also include radio observations of LGRB hosts (Perley & Perley 2013; Greiner et al. 2016; Perley et al. 2015; Peters et al. 2019) and SLSNe hosts (Hatsukade et al. 2018) from the literature. Shown for comparison are nearby dwarf galaxies from a number of surveys (Roychowdhury & Chengalur 2012; Hindson et al. 2018; Filho et al. 2019), as well as a sample of star-forming galaxies at $z \lesssim 0.5$ from the VLA-COSMOS source catalog (gray dots; Smolčić et al. 2017). Dashed lines indicate SFR$_{\rm radio}$ = SFR$_{\rm opt}$, 10 SFR$_{\rm opt}$, and 100 SFR$_{\rm opt}$.

We find that the late-time limits presented here probe a largely unexplored region of parameter space with timescales of $\delta t \gtrsim 10^3$ days and luminosities $L_\nu \sim 10^{28} - 10^{29}$ erg s^{-1} Hz^{-1}. With the exception of a few TDEs, most transients have been observed in the radio at earlier times. The radio limits for SLSNe are significantly fainter than the vast majority of cosmological GRBs, which are observed at earlier times ($\delta t \sim 1 - 10^3$ days) with luminosities $L_\nu \gtrsim 10^{30}$ erg s^{-1} Hz^{-1}. Conversely, the limits do not reach the levels of the least luminous SNe Ib/c with $L_\nu \sim 10^{26}$ erg s^{-1} Hz^{-1}. We explore the implications of these radio upper limits in the subsequent sections.

3. Obscured Star Formation

Measurements of SFRs as inferred from UV and optical data suffer from the obscuration effects of interstellar dust. At longer wavelengths, radio and millimeter observations offer a useful probe of star formation in dust-obscured galaxies as the emission arises from supernovae-accelerated cosmic-ray electrons and dust heating (Helou et al. 1985; Condon et al. 1991).

We place limits on the obscured SFRs in the host galaxies of our sample using the expression from Greiner et al. (2016), which extrapolates the 1.4 GHz derived SFR of Murphy et al. (2011) assuming a power law $F_\nu \propto \nu^\alpha$ and accounting for proper k-corrections:

$$\mathrm{SFR_{radio}} = 0.059\, M_\odot\ \mathrm{yr^{-1}}\, F_{\nu,\mu\mathrm{Jy}}\, d^2_{L,\mathrm{Gpc}}\, \nu^{-\alpha}_{\mathrm{GHz}} (1+z)^{-(\alpha+1)}, \quad (3)$$

where F_ν is the observed flux density at a frequency ν, and d_L is the luminosity distance at a redshift z. We adopt $\alpha = 0.75$ for the spectral index (Condon 1992).

In Figure 3, we compare the radio/millimeter-inferred upper limits on the SFR to the SFRs derived from Hα measurements or spectral energy distribution (SED) modeling (references are given

in the Appendix). We also plot radio observations of LGRB (Perley & Perley 2013; Perley et al. 2015; Greiner et al. 2016) and SLSNe (Hatsukade et al. 2018) hosts from the literature. For comparison, we include a sample of dwarf galaxies from a number of surveys (Roychowdhury & Chengalur 2012; Hindson et al. 2018; Filho et al. 2019), as well as star-forming galaxies at $z \lesssim 0.5$ from the VLA-COSMOS source catalog (Smolčić et al. 2017).

In the case of PTF12dam, our radio detection of the host galaxy corresponds to an SFR of $6.7 \pm 0.7\,M_{\odot}\,\mathrm{yr}^{-1}$, comparable to the value inferred from a previous 3 GHz detection ($4.8 \pm 0.2\,M_{\odot}\,\mathrm{yr}^{-1}$; Hatsukade et al. 2018) and an Hα measurement, $4.8 \pm 1\,M_{\odot}\,\mathrm{yr}^{-1}$ (Perley et al. 2016). This indicates that the star formation in the host is largely unobscured. X-ray emission is also detected near the location of PTF12dam (Margutti et al. 2018), which we conclude is likely related to the host. Finally, we note that the host galaxy of PTF12dam is among the brightest SLSNe hosts with strong emission lines and an absolute magnitude $M_g = -19.33$ (Chen et al. 2015).

Conversely, for PTF10hgi, Eftekhari et al. (2019) argue that the difference between the radio-inferred SFR of $2.3 \pm 0.3\,M_{\odot}\,\mathrm{yr}^{-1}$, and the optically inferred SFR of $0.09\,M_{\odot}\,\mathrm{yr}^{-1}$ indicates that the radio emission is not due to obscured star formation, but is instead related to the SN itself. The presence of weak emission lines from the host galaxy furthermore suggests that the system is not in an active starburst phase (Perley et al. 2016).

Finally, we note that the only remaining SLSN with a host galaxy radio detection is PTF10uhf (Hatsukade et al. 2018), in which the radio and optical SFR estimates are comparable, thus suggesting no dust obscuration as in the case of PTF12dam. Moreover, the host of PTF10uhf is unique relative to the population of SLSNe, with evidence of a merger between a large spiral galaxy and a less-massive disk galaxy (Perley et al. 2016). Indeed, when compared to the population of SLSNe host galaxies, the host of PTF10uhf is both among the most massive and the most prodigiously star-forming (Perley et al. 2016).

For the remaining SLSNe in our sample, the radio-inferred SFR limits exceed the optically inferred rates by factors of ≈ 2–5.2×10^3 (Table 4), where the high end is driven primarily by the ALMA 100 GHz observations, which are less constraining in this context. The median of the ratio of radio-to-optical SFRs for the VLA sample is < 32, indicating that there is no evidence for significant dust obscuration in these SLSN host galaxies.

We note that similar studies of SLSNe hosts in the radio are limited. Such studies include a search for radio emission from SLSNe host galaxies located within the footprints of wide-field radio surveys (Schulze et al. 2018); however, the survey rms levels do not provide particularly meaningful constraints. Deeper VLA observations of eight additional SLSNe show no evidence for dust attenuation (Hatsukade et al. 2018; Schulze et al. 2018).

Among the LGRBs in our sample, three overlap with the radio sample presented in Michałowski et al. (2012). The authors report 3σ limits for the SFRs at 1.4 GHz using the prescription of Bell (2003), which differs in normalization factor with our Equation (1). For consistency, we recompute their SFRs, finding $\mathrm{SFR_{radio}} < 6.5\,\mathrm{M_{\odot}\,yr^{-1}}$ (GRB 020903), < 21.0 (GRB 030329), and < 27.2 (GRB 061021). We improve on the limits for GRB 030329 and GRB 061021, finding $\mathrm{SFR_{radio}} < 2.5$ and < 13, respectively.

Limits on the radio-inferred SFRs for the host galaxies are roughly consistent with the optically derived SFRs (within a factor of a few to ten, with the exception of GRB061021 where the radio limit is a factor of $\sim$260 larger than the optical SFR), therefore ruling out significant dust obscuration in the hosts of the LGRBs for the majority of our sample.

To date, roughly 100 LGRB hosts have been observed in the radio, but the significant majority do not exhibit any discernible radio emission (e.g., Berger et al. 2001; Michałowski et al. 2015; Perley et al. 2015; Greiner et al. 2016). Radio-derived limits on the SFRs of these galaxies increasingly suggest little to no dust obscuration out to $z \approx 2$ (Michałowski et al. 2012; Perley et al. 2015; Greiner et al. 2016; although a small subset of the population, referred to as "dark" GRBs, exhibits significant extinction; Perley et al. 2013). Our limits are consistent with this scenario, allowing us to rule out significant dust obscuration for the majority of the LGRBs in our sample. We note that GRB 090417B is considered a heavily obscured, "dark" GRB (Perley & Perley 2013), where our radio-inferred SFR is a factor of 10 times larger than the optical rate.

Finally, we place tighter constraints on the mean radio and millimeter emission from each population (LGRBs and SLSNe) by stacking the individual images (excluding PTF12dam and PTF10hgi). We median-combine the images after centering on the transient position. We do not detect emission in either of the stacked populations, achieving 6 GHz rms values of about 2.6 and 1.9 μJy for LGRBs and SLSNe, respectively. The stacked ALMA image yields an rms of 3.7 μJy. We translate the rms values into limits on the mean obscured SFR, assuming the median redshift for each population. For the seven LGRBs in our sample, the non-detection corresponds to a 3σ limit of $\mathrm{SFR} \lesssim 4.2\ M_{\odot}\ \mathrm{yr}^{-1}$ ($z \approx 0.3$). For the SLSNe, the 3σ SFR limits are $\lesssim 1.7$ and $\lesssim 27\ M_{\odot}\ \mathrm{yr}^{-1}$ based on the 6 GHz ($z \approx 0.23$) and 100 GHz ($z \approx 0.23$) images, respectively.

4. Radio Emission from External Shocks

Radio observations of SNe provide a unique probe of the shock interaction between the ejecta and the surrounding circumstellar material (CSM; Chevalier 1982). This emission may arise from an initially off-axis relativistic jet that decelerates and spreads into the observer's line of sight at late times (Rhoads 1997; Sari et al. 1999), or from the fastest layers of the SN ejecta (Chevalier 1998).

In the case of SNe Ib/c, for example, the radio emission can be used to track the mass-loss history of the progenitor star (Soderberg et al. 2005, 2012; Wellons et al. 2012; Corsi et al. 2016; Palliyaguru et al. 2019). The precise mechanism by which material is removed from the progenitor remains an open question, though it is likely related to binary mass transfer, or for more massive stars, strong stellar winds (Woosley et al. 1995). In a small subset of events, there has been evidence for relativistic ejecta (Soderberg et al. 2010; Margutti et al. 2014).

The production of relativistic jets in LGRBs has been attributed to fallback accretion onto a black hole (MacFadyen & Woosley 1999; MacFadyen et al. 2001) or the rotational energy of a millisecond magnetar (e.g., Thompson et al. 2004; Metzger et al. 2011). Recently, Margalit et al. (2018b) argued that similar jets may accompany SLSNe, if they are powered by magnetars. In this scenario, a misalignment of the magnetar's rotation and magnetic axes leads to a partitioning of the magnetar's spin-down

Table 4
Source Parameters

Source	z	Explosion Date (MJD)	$\delta t_{6\ \mathrm{GHz}}$[a] (days)	$\delta t_{100\ \mathrm{GHz}}$[b] (days)	$F_{6\ \mathrm{GHz}}$ (uJy)	$F_{100\ \mathrm{GHz}}$ (uJy)	$\mathrm{SFR_{radio}}$[b] ($M_\odot\ \mathrm{yr}^{-1}$)	$\mathrm{SFR_{opt}}$ ($M_\odot\ \mathrm{yr}^{-1}$)
SN1999as	0.13	51172	6069	⋯	<20.01	⋯	<1.66	0.18
SN2005ap	0.28	53424	3631, 4135	⋯	<34.17, <6.71	⋯	<16.31	0.13
SN2006oz	0.38	54025	2896	2964	<20.22	<52.83	<18.30	0.13
SN2007bi	0.13	54075	3554	3653	<36.42	<53.10	<3.07	0.02
SN2009jh	0.35	55014	2288	⋯	<19.5	⋯	<15.00	<0.01
PTF09cnd	0.26	55006	2461	⋯	<18.54	⋯	<7.19	0.115
SN2010kd	0.10	55499	2321	⋯	<14.34	⋯	<0.73	0.0
SN2010gx	0.23	55251	2279	2341	<16.92	<57.12	<5.09	0.26
SN2011ke	0.14	55651	2135	⋯	<14.91	⋯	<1.59	0.44
SN2011kf	0.25	55921	1743, 2255	1787	<16.68, <13.86	<50.1	<4.79	0.15
SN2011kg	0.19	55912	1761	⋯	<18.9	⋯	<3.82	0.39
SN2012il	0.18	55919	1782, 2386	1858	<15.99, <15.96	<57.21	<2.64	0.40
PTF12dam	0.11	56022	1878, 2445	⋯	$117.2 +/-11.6, 61.5 \pm 10.8$[c]	⋯	6.75	4.8
LSQ12dlf	0.26	56119	1508	1592	<29.76	<51.18	<11.24	0.40
SSS120810	0.16	56116	⋯	1720	⋯	<51.87	<55.12	0.06
SN2013dg	0.27	56419	⋯	1353	⋯	<61.89	<10.15	0.4
LSQ14an	0.16	56513	⋯	1357	⋯	<48.33	<56.47	1.19
LSQ14bdq	0.35	56721	⋯	1031	⋯	<55.5	<340.83	0.16
LSQ14fxj	0.36	56882	⋯	907	⋯	<53.34	<360.76	0.74
LSQ14mo	0.25	56636	⋯	1174	⋯	<60.66	<185.77	0.52
CSS140925	0.46	56900	⋯	835	⋯	<50.79	<592.79	0.56
SN2015bn	0.11	57013	⋯	1003	⋯	<54.66	<29.47	0.04
OGLE15sd	0.57	57295	⋯	524	⋯	<36.24	<690.66	⋯
iPTF16bad	0.24	57513	⋯	1056	⋯	<42.18	<122.14	⋯
SN2016ard	0.20	57433	⋯	590	⋯	<59.79	<112.04	0.85
SN2016els	0.22	57543	⋯	1013	⋯	<60.48	<131.91	⋯
SN2017gci	0.09	57939	⋯	818	⋯	<46.17	<15.22	—
SN2017jan	0.40	57986	⋯	613	⋯	<64.38	<540.97	⋯
SN2018bsz	0.03	58203	⋯	615	⋯	<45.27	<1.22	0.5
SN2018ffj	0.23	58275	⋯	458	⋯	<53.43	<137.63	⋯
SN2018ffs	0.14	58324	⋯	415	⋯	<53.97	<46.85	⋯
SN2018gft	0.23	58355	⋯	386	⋯	<51.45	<127.58	⋯
SN2018hti	0.06	58415	⋯	403	⋯	<51.81	<8.12	0.39
SN2018ibb	0.16	58465	⋯	374	⋯	<57.57	<64.62	⋯
SN2018jfo	0.16	58411	⋯	376	⋯	<53.79	<62.85	⋯
SN2018lfe	0.35	58424	⋯	313	⋯	<62.04	<393.62	1.0
GRB020903	0.251	52884	4389	⋯	<19.80	⋯	<7.22	2.65
GRB030329	0.1685	52727	4557	⋯	<16.8	⋯	<2.54	0.71
GRB050826	0.296	53608	3398	⋯	<25.83	⋯	<10.21	1.17
GRB061021	0.3463	54029	2987	⋯	<17.25	⋯	<12.95	0.05
GRB090417B	0.345	54938	2343	⋯	<16.83	⋯	<12.55	1.25
GRB111225A	0.297	55920	1612	⋯	<18.00	⋯	<9.56	⋯
GRB120422A	0.283	56039	1567	⋯	<15.21	⋯	<7.25	1.65

Notes. Limits correspond to 3σ. Explanations of explosion dates and references for $\mathrm{SFR_{opt}}$ given in the Appendix.
[a] Explosion rest frame.
[b] We use the most constraining limit for sources with multiple observations.
[c] The host galaxy emission is resolved out in the second-epoch, A-configuration observations.

luminosity, where some fraction of the spin-down power is converted into thermal energy behind the SN ejecta, while the remaining power energizes a relativistic jet. Thus, sufficiently energetic jets may break through the SN ejecta, producing late-time radio afterglow emission from SLSNe.

Below we use our radio limits to place constraints on the radio emission from external shocks due to both nonrelativistic and relativistic outflows.

4.1. Supernovae Ejecta

In the context of a shock interaction from the nonrelativistic, quasi-spherical SN ejecta, we place limits on the shock velocity and mass-loss rate for each SLSN following the prescription of Chevalier (1998) and assuming that the date of each observation corresponds to the peak luminosity; see Figure 4. We also consider the possibility that the emission from each event may have peaked at earlier times, by extrapolating the peak luminosity back in time assuming $L_{\nu,\mathrm{pk}} \propto t^{-1}$ (Berger et al. 2002), and assuming that the emission is optically thin at the time of observations. This allows us to rule out the region of parameter space above each curve.

We find that in this context, our limits at late times do not probe the range of mass-loss rates and ejecta velocities inferred for SNe Ib/c, which have mostly been detected at early times,

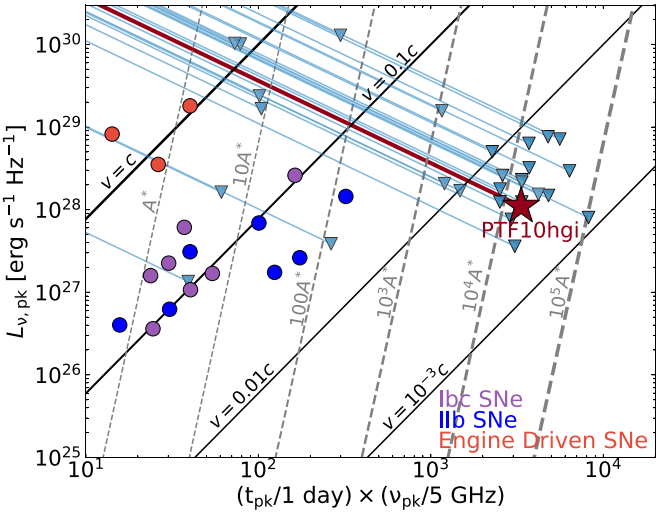

Figure 4. Peak radio luminosity ($L_{\nu,\rm pk}$) vs. the product of peak frequency and time ($\nu_{\rm pk} \times t_{\rm pk}$) for our sample of SLSNe (blue triangles), as well as all existing observations of SLSNe from the literature (see Table 1). Individual lines for each SLSN account for a possible peak at an earlier time assuming $L_{\nu,\rm pk} \propto t^{-1}$. Black and gray lines mark constant shock velocity and mass-loss rate, respectively, given the standard formulation for synchrotron self-absorbed emission from a freely expanding nonrelativistic blastwave (Chevalier 1998), with $\epsilon_B = \epsilon_e = 0.1$. Also shown is the 6 GHz detection for PTF10hgi (star; Eftekhari et al. 2019) as well as Type Ib/c (purple circles), IIb (blue circles), and engine-driven (red circles) SNe from the literature (Soderberg et al. 2005; Margutti et al. 2019).

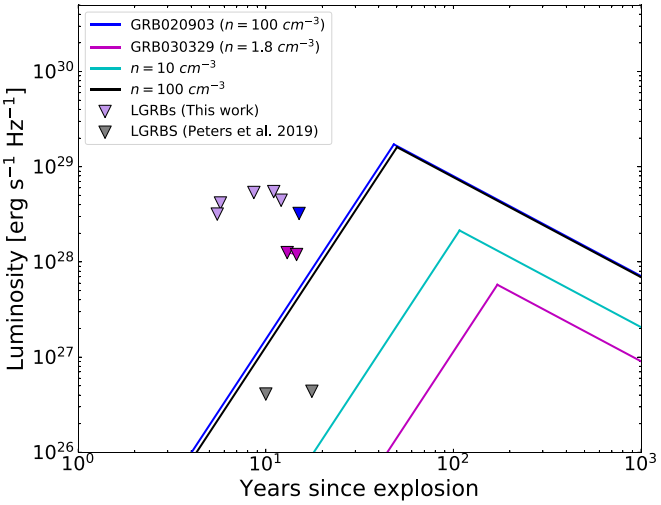

Figure 5. Model light curves at 6 GHz for associated SNe in LGRBs assuming values of $\epsilon_e = \epsilon_B = 0.1$, p=2.5, $E_{\rm SN} = 10^{52}$ erg, $v_{\rm ej} = 8 \times 10^3$ km s^{-1}, and external number densities $n = 10$ and $n = 100$ cm^{-3} compared to late-time limits presented in this work (light purple) and in Peters et al. (2019; gray). For GRB 020903 and GRB 030329, we plot unique models with $n = 100$ (blue) and $n = 1.8$ cm^{-3} (magenta) based on modeling of the GRB afterglows (Berger et al. 2003; Soderberg et al. 2004).

with typical inferred values of $v_{\rm ej} \sim 0.1$c and $A \sim 1$–$100\,A^*$ (e.g., Berger et al. 2002; Soderberg et al. 2005, 2012). On the other hand, a small number of SLSNe limits from the literature at earlier times probe the typical ejecta velocities and mass-loss rates inferred for SNe Ib/c, and thus suggest that comparable outflows are not ubiquitous in SLSNe. One possible exception is PTF10hgi, in which the radio detection would imply an ejecta velocity and progenitor mass-loss rate a few times larger than for SNe Ib/c. However, our interpretation for this event is that the radio emission is due to central engine activity.

For the LGRBs in our sample, we place constraints on emission from associated supernovae following the prescriptions of Barniol Duran & Giannios (2015) and Kathirgamaraju et al. (2016). In this scenario, radio emission is produced by a spherical outflow from the accompanying supernova, which peaks at the deceleration time ($t_{\rm dec}$), when the SN has swept up a mass comparable to the initial ejected mass. During this phase, the light curve rises as[21] $\propto t^3$ and decays after the deceleration time as $\propto t^{-3(1+p)/10}$. We assume typical values of $\epsilon_e = \epsilon_B = 0.1$ and $p = 2.5$. We also include in our analysis late-time observations of three LGRBs from Peters et al. (2019).

In Figure 5, we plot representative light curves for external number densities of $n = 10$ and $n = 100\,{\rm cm}^{-3}$ and a fiducial supernova energy of 10^{52} erg, typical of broad-line Ic SNe associated with GRBs (Mazzali et al. 2014). For GRB 020903 and GRB 030329, we plot individual curves corresponding to the inferred densities ($n = 100$ and $n = 1.8\,{\rm cm}^{-3}$, respectively) from modeling of the GRB afterglows (Berger et al. 2003; Soderberg et al. 2004). We further fix the ejecta velocity to $8 \times 10^3\,{\rm km\,s}^{-1}$, consistent with the median observed nebular-phase velocity for several broad-line Ic SNe (e.g., Mazzali et al. 2001, 2007b, 2007a).

[21] This is for the idealized scenario where the ejecta expands with a single velocity $v_{\rm ej}$ (see Kathirgamaraju et al. 2016 for an extension to this scenario).

We note that this is in contrast to Peters et al. (2019), in which the authors use the SN ejecta velocity at ~10 days after explosion, corresponding to velocities three to four times larger than the observed nebular velocities. This has a dramatic effect on the resulting light curves, which scale as $(v_{\rm ej}/c)^{(11+p)/2}$ at $t < t_{\rm dec}$. Indeed, we find that the light-curve luminosities are roughly an order of magnitude fainter than our LGRB limits on the same timescale assuming $n = 100\,{\rm cm}^{-3}$, with the exception of deep limits for GRB 060218 and GRB 980425 from Peters et al. (2019), which rule out these models, but cannot rule out densities $\lesssim 10\,{\rm cm}^{-3}$. Furthermore, imposing the lower inferred nebular-phase velocities shifts the peak of the light curves as $t_{\rm dec} \propto (v_{\rm ej}/c)^{-5/3}$ to $t_{\rm dec} \gtrsim 50$ yr, well beyond the timescale of our observations at $\delta t \sim 10$ yr. Finally, we note that even for a more promising choice of SN parameters (large ejecta velocity and energy) our radio nondetections may still be unconstraining due to inhibition of the early ($\lesssim$ decades) SN light curve that is predicted to be caused by interaction of the GRB jet with the interstellar medium (Margalit & Piran 2020).

We thus conclude that we cannot place strong constraints on associated SNe in our sample of LGRBs, but note that such sources may be detectable on timescales of a few decades if they occur in high-density ($n \approx 100\,{\rm cm}^{-3}$) environments. Lower densities will require deep radio observations on century timescales.

4.2. Off-axis Relativistic Jets

To constrain the presence of off-axis jets, we produce a grid of afterglow models for a range of jet energies and CSM densities using the two-dimensional relativistic hydrodynamical code `Boxfit v2` (van Eerten et al. 2012). We generate afterglow light curves at 6 and 100 GHz and compare these to our upper limits to determine the allowed region of parameter space for each event. We model the light curves assuming a jet opening angle of $\theta_j = 10°$ and viewing angles of $\theta_{\rm obs} = 30°$, 60°, and 90°. We further assume a constant-density CSM and jet microphysical parameters of $\epsilon_e = 0.1$, $\epsilon_B = 0.01$, and

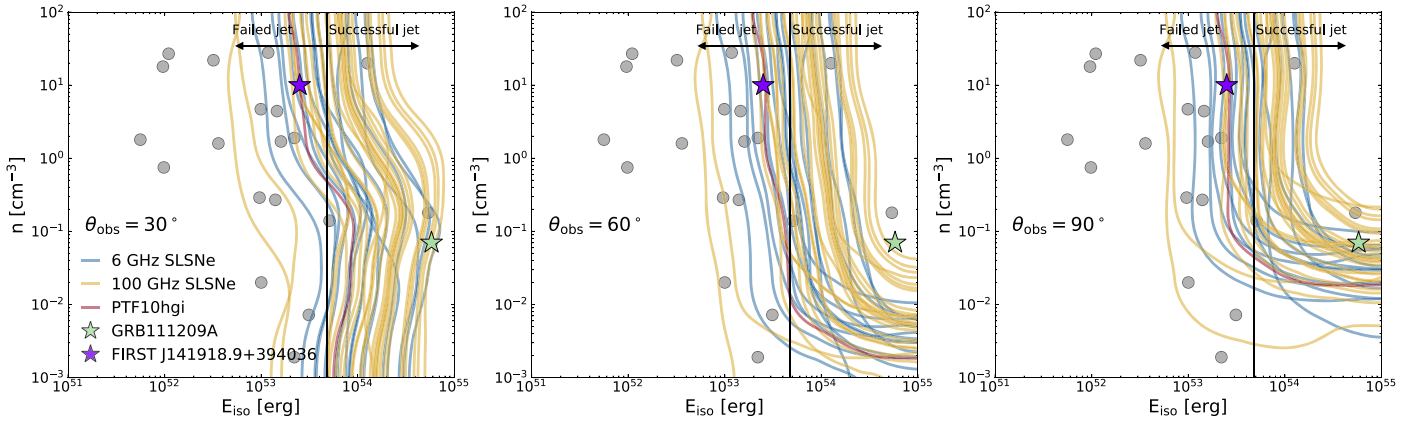

Figure 6. Constraints on the allowed jet energies and CSM densities for off-axis jets with an initial opening angle $\theta_j = 10^\circ$ and viewing angles of $\theta_{obs} = 30^\circ$, $\theta_{obs} = 60^\circ$, and $\theta_{obs} = 90^\circ$. Individual curves correspond to the allowed region of parameter space for each SLSN in our sample, where in each case the region to the right of the curve is ruled out by the 6 (blue) or 100 GHz (yellow) non-detection. Also shown are the range of jet energies and CSM densities consistent with the radio detection of PTF10hgi (Eftekhari et al. 2019). For comparison, we also include the extragalactic radio transient FIRST J141918.9+394036 (Law et al. 2018) and the ultra-long GRB 111209A (Stratta et al. 2013), as well as a sample of LGRBs (gray circles) from the literature (Berger et al. 2001; Panaitescu & Kumar 2002; Berger et al. 2003; Yost et al. 2003; Chevalier et al. 2004; Chandra et al. 2008; Cenko et al. 2010; Laskar et al. 2015). The vertical black line depicts the median jet breakout energy E_{min} from Table 5.

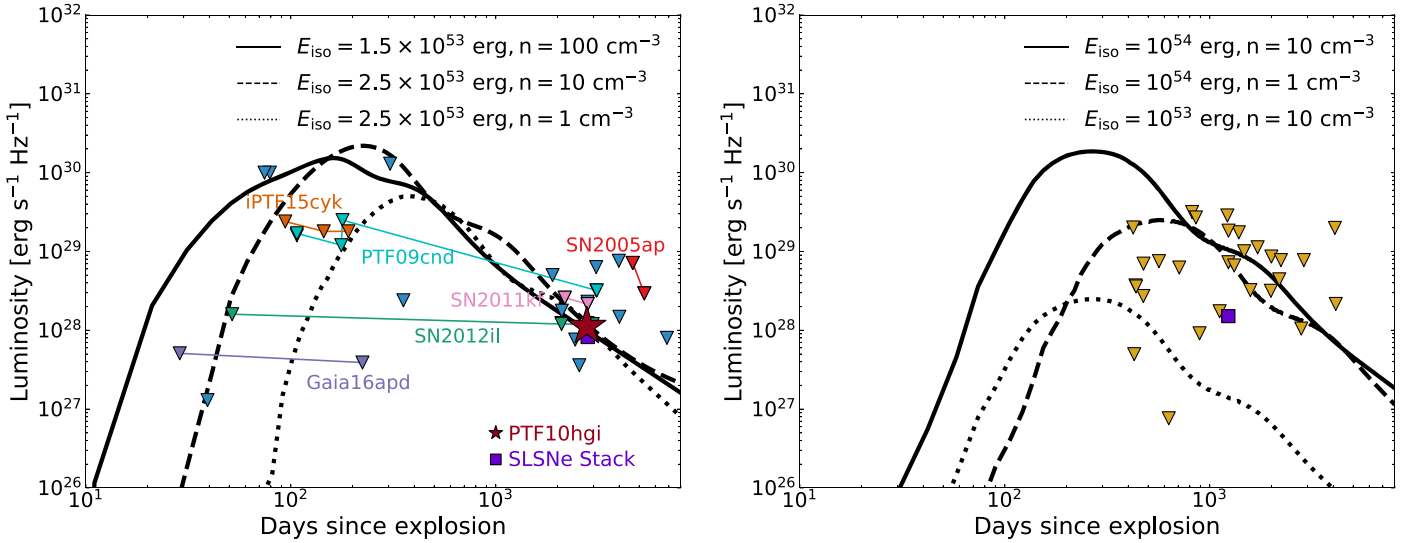

Figure 7. Left: off-axis jet light curves at 6 GHz for $\theta_{obs} = 60^\circ$ that are consistent with the radio detection of PTF10hgi. Individual curves depict a range of jet energies and CSM densities that can reproduce the observed flux density at $\delta t \sim 7.5$ yr (Eftekhari et al. 2019). Shown for comparison are existing limits for SLSNe between 5 and 9 GHz (see Table 1), where we highlight sources with multiple epochs of observations. Right: off-axis jet light curves at 100 GHz ($\theta_{obs} = 60^\circ$) compared to upper limits for our sample of events. We also plot in both panels the luminosity corresponding to the stacked 3σ limit assuming the median observer time and redshift of the VLA and ALMA samples, respectively.

$p = 2.5$, following previous studies of LGRBs (e.g., Curran et al. 2010; Laskar et al. 2013; Wang et al. 2015; Laskar et al. 2016; Alexander et al. 2017a).

The results are summarized in Figure 6, where individual curves trace the jet energies and CSM densities corresponding to the 3σ flux density limit for each SLSN. In each case, the region of parameter space to the right of the curve (higher energies) is ruled out by the 6 and 100 GHz nondetections. We find that the radio limits largely preclude the presence of jets with $E_{iso} \gtrsim 10^{54}$ erg ($n \sim 10^{-3}$–10^{2} cm^{-3}) for $\theta_{obs} = 30^\circ$ and 60°. For $\theta_{obs} = 90^\circ$, we cannot rule out jets with $E_{iso} \lesssim 10^{54}$ erg and $n \sim 10^{-3}$–10^{-2} cm^{-3}.

In Figure 7, we compare three representative off-axis jet light curves at 6 GHz to the limits for SLSNe, where we include all observations of SLSNe at 5–9 GHz from the literature (see Table 1). Individual curves depict jet energies of $E_{iso} = 1.5 - 2.5 \times 10^{53}$ erg and CSM densities $n = 1$–100 cm^{-3}, corresponding to a range of afterglow models that are consistent with the 6 GHz detection of PTF10hgi at $\delta t \sim 7.5$ yr (Eftekhari et al. 2019). We find that previous observations of SLSNe on timescales of a few hundred days post-explosion rule out the presence of jets with an energy scale similar to that inferred for PTF10hgi. Conversely, for the sample of SLSNe presented here, we generally cannot rule out the presence of similar jets, primarily because most of the SLSNe are located at larger distances than PTF10hgi.

We also plot off-axis jet light curves at 100 GHz and compare to our ALMA upper limits in the right-hand panel of Figure 7. Because the peak of the afterglow emission is generically at GHz frequencies on such long timescales, our millimeter limits can accommodate higher jet energies of $E_{iso} \gtrsim 10^{54}$ erg. This can also be seen in Figure 6, where the ALMA limits trace out generally higher energies than the 6 GHz limits. We note that the two most constraining limits in the entire sample correspond to the lowest redshift sources in

Table 5
SLSN Magnetar Parameters and CLOUDY Results

Source	P (ms)	B (10^{14} G)	$M_{\rm ej}$ ($M_\odot$)	E_K (10^{51} erg)	$v_{\rm ej}$ (10^3 km s^{-1})	$t_{\rm ff,\ 6\ GHz}$ (yr)	$t_{\rm ff,\ 100\ GHz}$[a] (yr)	$E_{\rm min,iso}$[b] (10^{51} erg)
SN2005ap	1.28	1.71	3.57	8.85	15.22	2.43	< 0.16	1108
SN2006oz	2.70	0.32	2.97	2.66	9.46	2.05	< 0.19	333
SN2007bi	3.92	0.35	3.80	2.37	7.90	5.94	1.94	297
SN2009jh	1.74	0.27	6.98	6.78	9.11	4.52	1.70	849
PTF09cnd	1.46	0.10	5.16	3.29	8.56	1.33	< 0.16	412
PTF10hgi	4.78	2.03	2.19	0.55	5.12	4.85	1.39	69
SN2010gx	3.66	0.59	2.39	3.78	12.65	3.63	1.24	473
SN2010kd[c]	3.51	0.57	10.51	3.64	5.90	16.13	4.43	456
SN2011ke	0.78	3.88	7.64	5.22	8.15	2.90	< 0.13	653
SN2011kf	1.48	0.70	4.57	6.72	11.46	3.11	< 0.15	841
SN2011kg	2.07	2.88	6.54	7.97	12.11	6.98	1.86	998
SN2012il	2.35	2.24	3.14	1.94	7.93	3.95	< 0.14	243
PTF12dam	2.28	0.18	6.27	3.03	7.01	4.28	1.81	379
LSQ12dlf	2.82	1.20	3.68	2.54	8.28	5.72	1.66	318
SSS120810	3.00	1.93	2.22	2.82	11.13	3.42	< 0.14	353
SN2013dg	3.50	1.56	2.75	1.85	8.38	5.19	1.50	232
LSQ14bdq	0.98	0.49	33.71	25.06	8.71	16.67	4.57	3137
LSQ14mo	4.97	1.01	2.10	2.43	10.74	4.77	1.44	304
SN2015bn	2.16	0.31	11.73	3.45	5.46	12.00	3.49	432
OGLE15sd	2.16	1.74	1.91	6.29	9.33	9.17	2.53	787
iPTF16bad	3.73	2.62	2.22	1.12	7.11	4.55	1.29	140
SN2016ard[d]	0.93	1.55	16.6	33.0	14.2	7.80	<2.11	4131
SN2016els[c]	0.92	5.38	11.83	28.0	15.43	5.50	1.39	3505
SN2017gci[c]	1.26	3.46	11.74	7.16	7.83	6.86	1.81	896
SN2017jan[c]	3.08	0.34	7.14	4.58	8.03	10.84	3.26	573
SN2018hti[c]	1.25	2.59	31.04	11.3	6.06	15.67	3.80	1415
SN2018ibb[c]	0.74	0.16	43.47	45.6	10.27	12.12	3.67	5708
SN2018lfe[e]	2.85	2.2	3.80	3.82	10.05	6.04	1.71	478

Notes. Magnetar parameters are from Nicholl et al. (2017c) except where specified. All times refer to the observer frame.
[a] We report upper limits where $t_{\rm ff,100GHz} < 1\ {\rm yr}(1+z)$, as these results are based on extrapolations to early times.
[b] Minimum energy required for a 10° jet to break out of the SN ejecta.
[c] Parameters derived in this work.
[d] From Blanchard et al. (2018).
[e] From Y. Yin et al. (2021, in preparation).

our sample, SN2018bsz and SN2018hti, which rule out off-axis jets with $E_{\rm iso} \gtrsim 10^{53}$ erg.

We further rule out a population of off-axis jets with an energy scale significantly larger than is seen in typical LGRBs (Figure 6). In this context, observations at earlier times ($\delta t \lesssim 1$ yr) are more constraining, as these probe the peak of the afterglow emission.

As noted in Margalit et al. (2018b), a successful jet will break out of the SN ejecta only if the jet head velocity exceeds the ejecta velocity, and if the kink stability criterion is satisfied, i.e., that magnetic energy is not dissipated due to kink instabilities (Bromberg & Tchekhovskoy 2016). These conditions lead to a minimum threshold energy for successful jet breakout given by:

$$E_{\rm min} \simeq 0.195\, E_K \left(\frac{\gamma_j}{2}\right)^{-4} f_j^{-1}, \quad (4)$$

where E_K is the initial kinetic energy of the SN, $\gamma_j = 1/5\theta_j$ as per Mizuta & Ioka (2013), and f_j is the fraction of energy contributing to a collimated jet (Margalit et al. 2018b). We assume $f_j = 0.5$ and adopt the inferred E_K values for each source based on fits to the optical light curves. For each SLSN in our sample,[22] we therefore estimate the minimal energy for jet breakout to determine whether our nondetections can constrain the theoretical predictions. The results are listed in Table 5.

Among our VLA sources, we find that four SLSNe (SN2010kd, SN2011ke, SN2011kf, and SN2011kg) have radio limits that preclude the presence of a relativistic jet. That is, for the afterglow model parameters specified above, the radio limits probe jet energies below $E_{\rm min}$. Thus, a successful jet produced by one of these sources would be readily detected in our observations. The remaining VLA sources have jet breakout energies that are not ruled out by our observations, and thus may harbor jets that are below the sensitivity of our observations, but with $E_{\rm iso} \gtrsim E_{\rm min}$.

Similarly, among our ALMA sources, we can rule out the presence of off-axis jets at an observer viewing angle $\theta_{\rm obs} \lesssim 30°$ for 13 sources (SSS120810, SN2013dg, LSQ14bdq, LSQ14mo, OGLE15sd, SN2015bn, SN2016ard, SN2016els, SN2017gci, SN2017jan, SN2018hti, SN2018ibb, and SN2018lfe) given that the jet breakout energy is ruled out by our 3σ radio limits. For SN2016ard, we further rule out all jets with $\theta_{\rm obs} \lesssim 60°$, as well as jets with $\theta_{\rm obs} \lesssim 90°$ and $n \gtrsim 10^{-2}\,{\rm cm}^{-3}$. Similarly, for LSQ14bdq, SN2016els, and SN2018ibb, we can rule out $\theta_{\rm obs} \lesssim 60°$ and $n \gtrsim 10^{-2}\,{\rm cm}^{-3}$ and $\theta_{\rm obs} \lesssim 90°$ and $n \gtrsim 10^{-1}\,{\rm cm}^{-3}$. For SN2017gci and SN2018hti, we can rule out all jets with $\theta_{\rm obs} \lesssim 60°$ and jets

[22] For this calculation, we use only the sources with estimates of E_K as derived from fits to the optical light curves using the Modular Open-Source Fitter for Transients (MOSFIT; see Table 5).

with $\theta_{\rm obs} \lesssim 90°$ and $n \gtrsim 10^{-1}\,{\rm cm}^{-3}$. Thus, for SN2016ard, LSQ14bdq, SN2016els, SN2018ibb, SN2017gci, and SN2018hti, the allowed phase-space for a successful jet that is not ruled out by our observations is prohibitively small.

Finally, we note that the range of jet breakout energies ($E_{\rm min,iso} \approx 7 \times 10^{52}$–$6 \times 10^{54}$ erg) for the SLSNe in our sample suggests that we do not expect a population of off-axis jets with energies comparable to the lowest-energy LGRBs, e.g., $E_{\rm iso} \lesssim 10^{53}$ erg, given that such jets will fail to break out of the SN ejecta.

5. Magnetar Wind Nebulae

In the standard pulsar wind scenario, a newly formed neutron star acts as an energy reservoir for relativistic electron/positron pairs, leading to the production of a magnetized outflow, or pulsar wind nebula (PWN), inflated behind the expanding SN ejecta (Gaensler & Slane 2006). Relativistic particles in the nebula are accelerated into a power-law distribution, producing nonthermal synchrotron radiation across the electromagnetic spectrum. In the GHz frequency regime, this emission is expected to penetrate the surrounding SN ejecta on timescales of several years to decades (Murase et al. 2016; Omand et al. 2018), as the ejecta becomes optically thin to free–free absorption and synchrotron self-absorption.

To model the PWN radio emission from each newborn SLSN remnant, we use the inferred magnetar birth properties (ejecta mass and velocity, magnetar magnetic field, and spin period) from Nicholl et al. (2017c) and Blanchard et al. (2018), and in a few cases presented here (see Table 5). The parameters are derived via Markov Chain Monte Carlo fits to the multicolor light curves using `MOSFiT`, an analytic Python-based modular code designed to model a variety of transients. We note that other approaches to modeling the optical light curves of SLSNe may lead to different parameter estimates (e.g., Omand et al. 2018; Law et al. 2019). Such studies use a spin-down formula based on numerical simulations (Gruzinov 2005; Spitkovsky 2006; Tchekhovskoy et al. 2013), which gives a factor $3(1 + C \sin^2 \chi_\mu)/2 \sin^2 \chi_\mu \sim 5$ larger spin-down luminosity for a given P and $B_\perp$ (χ_μ here is the angle between the magnetic and rotational axes, and $C \sim 1$ is a numerical prefactor; Kashiyama et al. 2016; Omand et al. 2018) . These models also allow for the pressure of the PWN to accelerate the SLSN ejecta, effectively coupling the ejecta kinetic energy to the spin-down luminosity of the magnetar. These approaches may lead to differences in the resulting light curves and parameters. We note however that a systematic comparison of these methods is beyond the scope of this work.

Before computing the predicted PWN radio light curves for each source, we first assess the likelihood of detection for each SLSN in our sample[23] by computing the free–free optical depth through the SN ejecta, and hence the transparency timescale for radio emission. Using the photoionization code `CLOUDY` (Ferland et al. 2013), we compute the time-dependent evolution of the temperature and ionization structure of the ejecta assuming that some fraction of the spin-down power of the magnetar is deposited into ionizing radiation. The ejecta density distribution for each SLSN is set by the inferred magnetar parameters. Assuming that the energy injection rate into the nebula is given by $L \propto t^{-2}$, we find $t_{\rm ff} \approx 1.3$–16.7 yr at 6 GHz and ≈ 1.2–4.6 yr at 100 GHz. We therefore find that the majority of our sources are expected to be optically thin to radio emission at the time of our observations, with the exception of nine sources; SN2011kg and LSQ12dlf are expected to be optically thick at the time of our 6 GHz observations, while LSQ14bdq, SN2015bn, SN2016ard, SN2017jan, SN2018ibb, SN2018hti, and SN2018lfe are expected to be optically thick in our 100 GHz observations. This is consistent with the fact that these sources have larger inferred ejecta masses, and hence column densities, than the majority of SLSNe (with the exception of LSQ12dlf and SN2018lfe, which fall below the median ejecta mass of the SLSNe distribution). Finally, we report upper limits on $t_{\rm ff,\ 100GHz}$ for eight sources where $t_{\rm ff,\ 100GHz} > 1$ yr $(1+z)$, as the `CLOUDY` models start from $t > 1$ yr in the source frame, and these results are thus based on extrapolations.

Next, we constrain the presence of nascent magnetar nebulae in our sources following two unique prescriptions. First, we consider the scenario presented in Margalit & Metzger (2018; see also Beloborodov 2017), which posits an ion–electron wind produced by a young magnetar as the source of the radio emission for the quiescent counterpart associated with FRB 121102 (Kashiyama & Murase 2017; Metzger et al. 2017). Second, we consider an electron–positron wind, typical of standard PWNe, following the prescription of Omand et al. (2018). In both cases, we use the engine and ejecta properties inferred from `MOSFiT` as described above.

5.1. Ion–Electron Wind

Margalit & Metzger (2018) proposed a magnetized ion–electron wind from a young magnetar to explain the observed properties of FRB 121102, namely the size and flux of the persistent radio counterpart, as well as the large and decreasing RM of the bursts. The model assumes a one-zone nebula in which the magnetar's magnetic energy leads to the injection of relativistic electrons and ions that are thermalized at the termination shock of the magnetar wind. The model is characterized by the magnetic energy of the magnetar (E_{B_*}), the nebula velocity (v_n), the rate of energy input into the nebula ($t^{-\alpha}$) following the onset of the active period (t_0), the magnetization of the outflow (σ), and the mean energy per particle (χ) assuming a proton–electron composition. An ion–electron plasma composition is invoked given that the RM contribution of an electron–positron plasma is zero and thus inconsistent with the large observed RM (Michilli et al. 2018).

In Figure 8, we plot models A and B from Margalit & Metzger (2018), corresponding to inferred source ages of $t_{\rm age} \approx 12.4$ and 38 yr, respectively. In each case, the emission is expected to peak in the millimeter regime on timescales of a few years, and in the gigahertz regime on timescales of $\gtrsim 10$ yr. Moreover, the models predict 6 GHz luminosities of $\sim 10^{29}\,{\rm erg\,s^{-1}\,Hz^{-1}}$, consistent with the luminosity of the FRB 121102 persistent radio source (Chatterjee et al. 2017). We find that our limits at both 6 and 100 GHz are sufficient to rule out these models, *with the same parameters as for FRB 121102*.

We further compare our limits to the models used to describe the 6 GHz radio detection and 100 GHz upper limit of PTF10hgi from Eftekhari et al. (2019; see Figure 8). The first model is identical to model A for FRB 121102 from Margalit & Metzger (2018) with the magnetic energy scaled down by a factor of ≈ 20, while the second model explores a scenario in which the 6 GHz emission is marginally self-absorbed. In

[23] We perform this exercise exclusively for the sources listed in Table 5 as these events have the relevant engine and ejecta parameters from the `MOSFIT` models.

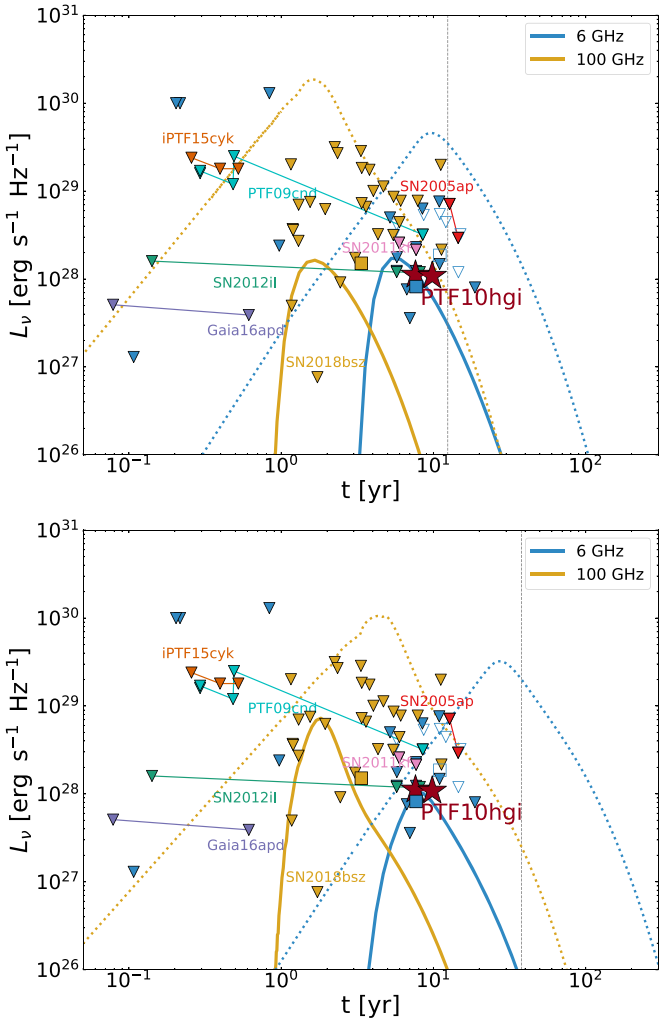

Figure 8. Ion–electron nebula models at 6 GHz (blue) and 100 GHz (yellow) based on the prescription for FRB 121102 from Margalit & Metzger (2018) compared to upper limits on the radio luminosity for SLSNe, LGRBS, and the 6 GHz detection of PTF10hgi (Eftekhari et al. 2019). Yellow symbols correspond to our ALMA 100 GHz upper limits, blue filled symbols correspond to all limits for SLSNe between 5 and 9 GHz, and blue open symbols indicate LGRBs. The stacked 3σ luminosity for each population assuming the median observer time and redshift are plotted using square symbols. Also shown are existing limits for SLSNe between 5 and 9 GHz. The dashed curves correspond to models A (top panel) and B (bottom panel) used to describe FRB 121102 from Margalit & Metzger (2018), where the vertical dashed line in each panel represents the presumed age of FRB 121102 in each model. The solid lines depict models that are consistent with the PTF10hgi detection at 6 GHz. Top: model A from Margalit & Metzger (2018; dashed lines). The solid lines show the same model but with the magnetic energy scaled down by a factor of ≈ 20 (i.e., $E_{\rm B_*} = 2.3 \times 10^{49}$ erg) to explain the 6 GHz detection of PTF10hgi. Bottom: model B from Margalit & Metzger (2018; dashed lines). The solid lines correspond to a synchrotron self-absorbed nebula that is consistent with the 6 GHz detection and 100 GHz limit for PTF10hgi as in Eftekhari et al. (2019).

Eftekhari et al. (2019), we showed that a fully self-absorbed nebula (as constrained by the 100 GHz non-detection) is also consistent with the data. However, recent results presented by Mondal et al. (2020) constrain the self-absorption frequency to $\sim$1 GHz based on a steep drop in flux density between 0.6 and 1 GHz. Indeed, we find that the predicted light-curve evolution of a marginally self-absorbed nebula is more consistent with the observed evolution of the 6 GHz luminosity.

We find that the majority of our limits are consistent with the model light curves invoked for PTF10hgi, although several deep limits at 100 GHz, most notably SN2018bsz with $L_\nu = 7.6 \times 10^{26}$ erg s^{-1} Hz^{-1}, strongly rule out the presence of such nebulae. We note that SN2018bsz exhibits unusual properties, including a pre-maximum plateau in the optical light curve in addition to strong carbon lines, which suggest that it may be an atypical event among SLSNe (Anderson et al. 2018). Although the timescale of our observations probes the predicted peak of emission, the sensitivity of our VLA and ALMA observations is not sufficient to rule out emission at the level of $L_\nu \lesssim 10^{28}$ erg s^{-1} Hz^{-1}. Thus, if ion–electron nebulae similar to the one inferred for PTF10hgi are ubiquitous in SLSNe, such sources will require deep radio observations, and may be more readily detected with future instruments such as the Square Kilometer Array.

It is worth noting however that PTF10hgi is among the nearest sources in our sample with $z = 0.0987$. Thus our nondetections for the remainder of the events may be indicative of their distance. Only two sources are located at lower redshifts: SN2018hti and SN2018bsz with $z = 0.063$ and $z = 0.027$, respectively, both of which are observed at 100 GHz. In the case of SN2018hti, we find that the SN ejecta is optically thick to 100 GHz emission at the time of our observations, while magnetar parameters have not been derived for SN2018bsz. In this context, a non-detection for SN2018hti is thus unsurprising, while nondetections for the remaining events may simply point to their greater distance relative to PTF10hgi.

Finally, the fact that the SLSNe radio limits preclude FRB 121102 models suggests that there may be physical differences (e.g., magnetic field strength) between the magnetar engines responsible for powering SLSNe and that inferred for FRB 121102.

5.2. Electron–Positron Wind

Here we consider a modified version of the PWN model presented in Omand et al. (2018; see also Murase et al. 2020), following the prescription of Murase et al. (2016) for quasi-steady radio emission from magnetar engines in SLSNe and FRBs. An electron–positron wind nebulae has also been considered to explain the observed properties of FRB 121102 (Murase et al. 2016; Kashiyama & Murase 2017). In this work, we modify the spin-down formula and neutron star masses, and ignore the effects of ejecta feedback for consistency with the MOSFiT models. The radio models solve the Boltzmann equation for photons and electron/positrons in the PWN over all photon frequencies and electron energies (Murase et al. 2015), allowing for a self-consistent calculation of pair cascades, Compton and inverse Compton scattering, adiabatic cooling, and both internal and external attenuation. The electron–positron injection spectrum is assumed to be a broken power law with injection spectral indices of $q_1 = 1.5$ and $q_2 = 2.5$ and a peak Lorentz factor of $\gamma_b = 10^5$, which is consistent with Galactic PWNe (e.g., Tanaka & Takahara 2010, 2013) such as the Crab PWN, as well as the inferred nebula for PTF10hgi with $q_1 = 1.3$ (Mondal et al. 2020). Free–free absorption in the ejecta is calculated assuming a singly ionized oxygen ejecta, and we do not consider absorption outside the ejecta, as in Omand et al. (2018) and Law et al. (2019).

The results of the models are shown in Figure 9 where we plot the predicted light curves at 6 and 100 GHz for the SLSNe in our sample with existing MOSFiT parameters (Table 5). The

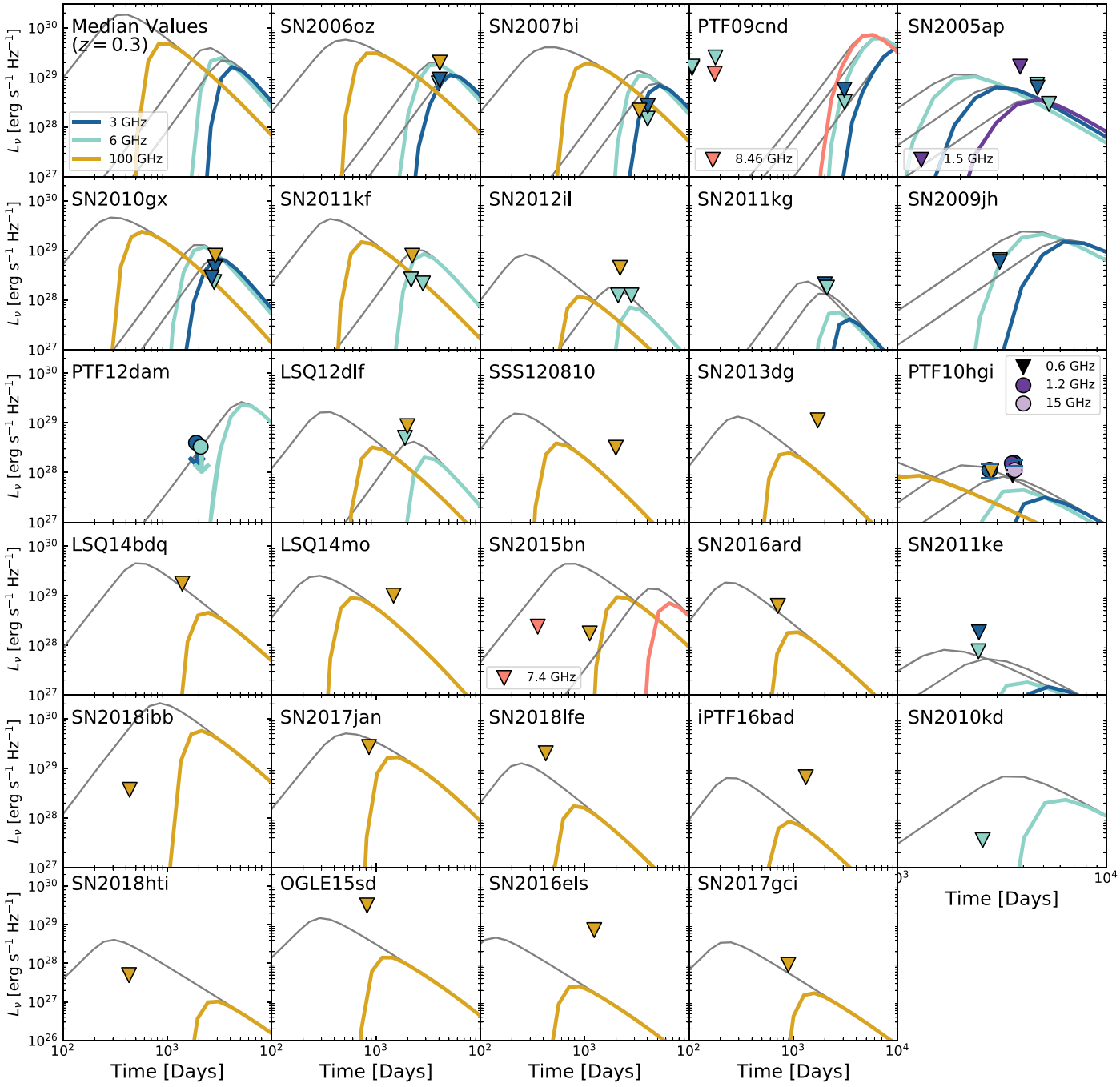

Figure 9. Radio and millimeter light curves at 6 and 100 GHz for electron–positron PWNe following the methods of Murase et al. (2016) and Omand et al. (2018). Light curves are shown for all SLSNe with existing MOSFiT magnetar parameters as given in Table 5. Gray curves indicate models with no absorption. The top left panel depicts the predicted radio light curve assuming the median magnetar parameters for the sample of SLSNe presented in Nicholl et al. (2017d). In a few cases, we also include data at nearby frequencies from the literature (Table 1), as well as models at 3 GHz for comparison to the models presented in Law et al. (2019). For PTF12dam, we adopt the host galaxy detection values as an upper limit. Limits correspond to 3σ.

models generically predict emission that peaks initially in the millimeter regime with an increased flux density on timescales of ∼1000 days and cascades to lower frequencies and lower flux densities at later times. In this context, the timescales of our ALMA observations lead to less constraining limits, as they do not probe the peak of the emission, which is expected at earlier times. In a few cases, we also include models at 3 GHz for comparison to limits and models presented in Law et al. (2019). We generate new 3 GHz models using the formalism described above for self-consistency.

For the majority of our sources, we find that the nondetections are consistent with the predicted light curves. At 6 GHz, a number of sources are expected to peak at later times relative to the timescale of our observations, and hence may be detected in the future with continued monitoring. We note that five sources exhibit predicted emission at or above the level of our 3σ limits at the time of our observations. This includes SN2006oz, PTF09cnd, and SN2011kf at 6 GHz, SN2010gx at 3 and 6 GHz, and SN2007bi at 3, 6, and 100 GHz. For an additional six sources (SN2009jh, SN2010kd, SN2012il, SN2017jan, SN2018ibb, and

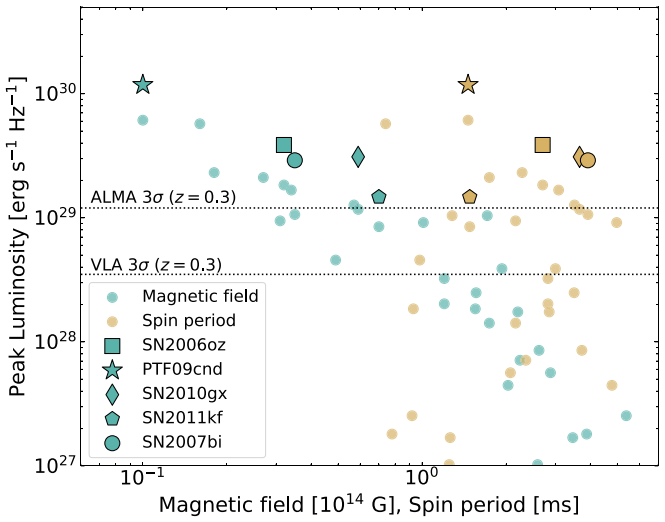

Figure 10. Peak model luminosities (assuming maximal absorption) at 6 and 100 GHz based on the electron–positron PWN light curves in Figure 9 as a function of magnetar magnetic field and spin period. We highlight individual sources that indicate predicted emission at or above the level of our 3σ limits at the time of our observations. Horizontal lines correspond to the typical 3σ sensitivity of our VLA and ALMA observations assuming $z = 0.3$.

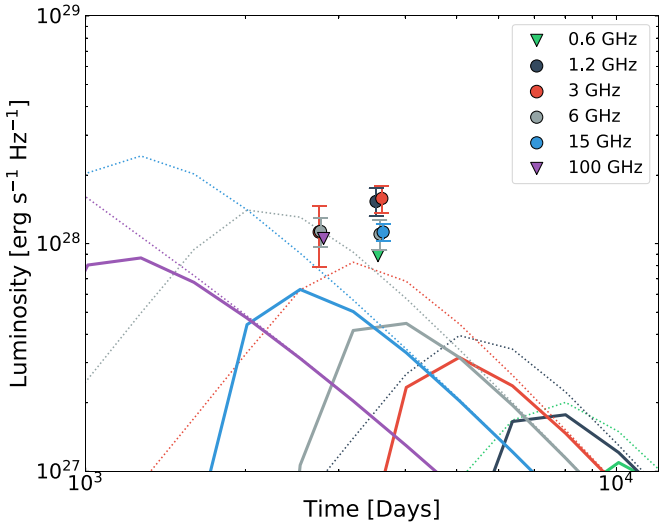

Figure 11. Electron–positron nebula model light curves for PTF10hgi at 0.6 − 100 GHz (Section 5.2) compared to the data from Eftekhari et al. (2019), Law et al. (2019), and Mondal et al. (2020). The dashed curved lines correspond to models without absorption.

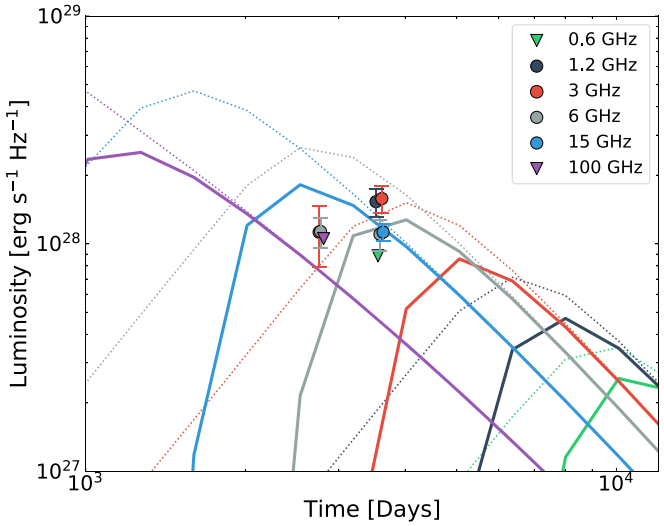

Figure 12. Electron–positron nebula models for PTF10hgi as in Figure 11, but with a peak Lorentz factor of $\gamma_b = 10^4$.

SN2018hti), the limits exclude models without absorption but cannot rule out models with absorption.

In Figure 10, we plot the predicted peak luminosity for each SLSNe (assuming maximal absorption) as a function of the inferred SLSN magnetic field and spin period. We find a strong anticorrelation between the peak luminosity and magnetic field, i.e., the more luminous events correspond to lower magnetic fields. This is consistent with the fact that the assumed pulsar spin-down luminosity $L_{\rm em} \propto B^{-2}$ as per numerical simulations (Gruzinov 2005). Indeed, the five sources with predicted emission at or above the level of our 3σ limits correspond to exclusively low-B ($B \lesssim 10^{14}$ G) events. Interestingly, from Figure 10, we also find that our VLA and ALMA observations are sensitive to a large fraction of low-B events, and thus indicate that continued monitoring on the appropriate timescales may reveal emission from these sources. Conversely, we find no clear correlation between the peak luminosity and the spin period.

For PTF10hgi, we plot the light curves over the range 0.6–100 GHz in Figure 11. We find that the observations at 6 GHz at $\delta t \approx 8$ yr (Eftekhari et al. 2019) are consistent with the model with no absorption, while the same models underpredict the data at $\delta t \approx 10$ yr (Mondal et al. 2020). At 3 GHz, the models slightly underpredict the data at $\delta t \approx 8$ yr (Law et al. 2019); however, this difference is negligible in light of systematic uncertainties. The 3 GHz light curve is predicted to rise between $\delta t \approx 8$–10 yr, consistent with the shape of the observed data, but with a scale significantly below the observations. Nondetections at both 0.6 and 100 GHz are consistent with the models. Conversely, the data at 1.2 and 15 GHz lie well above the predicted light curves.

In Law et al. (2019), the authors use unique magnetar parameters for PTF10hgi ($B = 1.4 \times 10^{14}$ G, $P = 1$ ms, $M_{\rm ej} = 15\,M_\odot$ based on by-eye estimates), and find that a model in which $\sim 40\%$ of the ejecta is singly ionized is consistent with the observed data. However, such a model fails to accurately predict the latest SED obtained in Mondal et al. (2020). Namely, the models slightly underpredict the data at 1.2–6 GHz, but vastly underpredict the data at 15 GHz. This is in contrast to the models presented here in which the low-frequency model at 1.2 GHz drastically underpredicts the observed flux value. This suggests that the true magnetar parameters may lie somewhere between the inferred values in both models (e.g., $P \approx 2$–4 ms, $M_{\rm ej} \approx 6$–9 $M_\odot$). On the other hand, the flat shape of the SED at 1–15 GHz may indicate a steeper injection spectrum, or an ionization fraction that evolves as a function of time. Continued broadband radio monitoring will provide a test of these scenarios.

In Figure 12 we plot the same data and models, but with a peak Lorentz factor of $\gamma_b = 10^4$ instead of 10^5; we find that these light curves are more consistent with the data. Specifically, we find that the models are below the nondetection upper limits at 0.6 and 100 GHz, and are consistent with the 3 GHz observations assuming no absorption and with the 6 GHz observations assuming partial absorption at $\delta t \approx 6$ yr and almost maximal absorption at $\delta t \approx 8$ yr. The models are consistent with the data at 15 GHz regardless of absorption (the ejecta are predicted to be optically thin for free–free absorption

at 15 GHz at the relevant timescale). Conversely, the model vastly underpredicts the 1.2 GHz data, which are predicted to peak at later times.

One interesting physical implication of decreasing γ_b is that the pair multiplicity in PTF10hgi is significantly higher than that of the Crab pulsar or other Galactic PWNe, which may indicate that the pair formation or acceleration processes in the nebulae of supernovae driven by highly magnetic millisecond pulsars are qualitatively different than those of Galactic PWNe. Nevertheless, it is unclear whether this is unique to SLSNe nebulae due to the luminosity of the nebula and strength of the pulsar field, or if SLSNe nebulae eventually evolve to have a lower multiplicity.

6. Conclusions

We presented the largest and deepest sample of radio and millimeter observations of SLSNe to date. Using the VLA and ALMA, our observations probe nonthermal synchrotron emission from these SLSNe, as well as a small sample of nearby LGRBs, on timescales of ∼1–19 yr post-explosion. Combined with existing observations from the literature, we place constraints on obscured star formation in the host galaxies, nonrelativistic ejecta, central engines, and the possible connection to FRBs. Our key results are summarized as follows:

1. We do not detect FRBs from any of our sources, placing limits on the maximum burst energies of $E_{\rm b,max} \lesssim 2 \times 10^{37}$–$4 \times 10^{38}$ erg, comparable to the lowest-energy bursts detected from FRB 121102 (Gourdji et al. 2019). However, the likelihood of a detection in such short-duration observations (∼40 minutes) is low, particularly in light of the intermittent nature of FRB 121102. Thus, further follow-up and a larger time investment with GBT, Arecibo, or FAST is warranted.
2. We find no evidence for significant dust obscuration within the host galaxies. PTF12dam is the only host that is detected in the radio, with a corresponding SFR of $\approx 7\,M_\odot\,{\rm yr}^{-1}$, consistent with the results presented in Hatsukade et al. (2018), and comparable to the Hα inferred rate of $\approx 5\,M_\odot\,{\rm yr}^{-1}$. Thus there is no indication of significant dust attenuation within the host galaxy. For the remainder of the SLSN hosts, we find that the radio-inferred SFR upper limits exceed optical estimates by factors of ≈ 2–5×10^3. Although some of our limits do not provide meaningful constraints in this context, for the majority of events, we can rule out significant dust obscuration in the SLSNe host galaxies. This is consistent with previous findings that indicate an absence of highly reddened SLSNe (Schulze et al. 2018).
3. In the context of nonrelativistic outflows (in analogy with SNe Ib/c), our late-time limits place direct constraints on low ejecta velocities ($v_{\rm ej} \approx 10^2$–$10^3\,{\rm km\,s^{-1}}$) and large CSM densities ($A \approx 10^3$–$10^5 A_*$). Extrapolating our limits back to earlier times (when SNe Ib/c are typically detected), we find that the inferred radio luminosities are roughly an order of magnitude larger than radio-detected SNe Ib/c. This suggests that SLSNe may indeed produce nonrelativistic outflows typical of SNe Ib/c. Such constraints will require deep radio observations of SLSNe at earlier times, of which there are currently only a small number.
4. For the LGRBs in our sample, we constrain the emission from associated supernovae, which is expected to peak at late times. We find that the low nebular-phase velocities of broad-line Ic SNe imply faint radio emission at the level of a few $\times 10^{27}$–$10^{29}\,{\rm erg\,s^{-1}\,Hz^{-1}}$, which peaks on timescales of several decades to centuries, well beyond the timescale of our observations. We therefore cannot place strong constraints on associated SNe in our sample of LGRBs, but note that such sources may be detectable at later times, particularly if they occur in high-density ($n \approx 100\,{\rm cm^{-3}}$) environments.
5. Our constraints on emission from off-axis relativistic jets allow us to rule out jets with $E_{\rm iso} \gtrsim 10^{54}$ erg for $\theta_{\rm obs} \lesssim 60°$ and a wide range of CSM densities ($n \sim 10^{-3} - 10^2\,{\rm cm^{-3}}$). For extreme off-axis viewing angles ($\theta_{\rm obs} \sim 90°$), we cannot rule out energetic jets with $E_{\rm iso} \gtrsim 10^{54}$ and low densities of $n \sim 10^{-3}$–$10^{-2}\,{\rm cm^{-3}}$. We also estimate the minimum energy required for a jet to break out of the SN ejecta from each source and find that the range of breakout energies, $E_{\rm min,iso} \approx 7 \times 10^{52}$–$6 \times 10^{54}$ erg, precludes a population of off-axis jets with energies comparable to the lowest-energy LGRBs ($E_{\rm iso} \lesssim 10^{53}$ erg), as such jets will fail to break out of the SN ejecta.
6. Our limits are sufficient to rule out the presence of ion–electron magnetar nebulae with the same parameters invoked for FRB 121102, as they probe luminosities roughly an order of magnitude deeper. On the other hand, we find that the majority of our limits are consistent with the same models tuned to the radio detection of PTF10hgi. This may point to some differences (e.g., magnetic field strength) between the magnetar engine powering FRB 121102 and those found in SLSNe.
7. In the context of an electron–positron PWN with an energy injection spectrum based on Galactic PWNe, we find that the majority of our nondetections are consistent with the predicted light curves, which peak at later times or are below the nominal sensitivity of our observations. On the other hand, the models for a small number of events predict emission at or above the level of our limits. These events correspond to exclusively low-B sources, with $B \lesssim 10^{14}$ G. Such discrepancies may reflect a time-varying ionization state or point to uncertainties in the inferred magnetar parameters.
8. A standard electron–positron PWN is unable to explain the observed spectrum for PTF10hgi. Namely, using the inferred engine parameters presented here, the light curve at 1.2 GHz significantly underpredicts the observed data. This is in contrast to the models presented in Law et al. (2019), which use unique engine parameters and subsequently underpredict the data at 15 GHz. This suggests that the true engine parameters may lie somewhere between the inferred values in both models. Conversely, the ionization fraction of the ejecta may evolve as a function of time, or the energy injection spectrum may be steeper than assumed. We further decrease the peak Lorentz factor to $\gamma_b = 10^4$ and find that the resulting light curves are somewhat more consistent with the data, yet still unable to explain the full SED of PTF10hgi. A decrease in γ_b would imply a significantly higher pair multiplicity in PTF10hgi relative to Galactic PWNe.

Continued radio monitoring of these sources on timescales of 5–10 yr may lead to detections, particularly in the context of PWNe models, which predict that the 6 GHz emission will peak at even later times. At 100 GHz, improved constraints will

require both earlier observations and in many cases increased sensitivity, to probe the levels of emission associated with PWNe. In this context, targeting nearby SLSNe with small inferred B-values may provide the fastest route to a detection. Conversely, constraints on jetted emission predicate the need for multiple epochs of observations, as these are more constraining on the allowed region of parameter space with respect to observer angles, jet energies, and CSM densities. Finally, continued searches for FRBs from these sources may lead to detections, establishing a connection between FRBs and SLSNe and/or LGRBs.

We thank the referee for the thoughtful comments and suggestions which helped to improve the manuscript. The Berger Time-Domain Group at Harvard is supported in part by the NSF under grant AST-1714498. S.C. and J.M.C. acknowledge support from the National Science Foundation (AAG-1815242). M.N. is supported by a Royal Astronomical Society Research Fellowship. C.M.B.O. has been supported by the Grant-in-aid for the Japan Society for the Promotion of Science (18J21778). K.D.A. acknowledges support provided by NASA through the NASA Hubble Fellowship grant HST-HF2-51403.001 awarded by the Space Telescope Science Institute, which is operated by the Association of Universities for Research in Astronomy, Inc., for NASA, under contract NAS5-26555. R.M. acknowledges partial support by the National Science Foundation under award No. AST-1909796 and AST-1944985 and by the Heising-Simons Foundation under grant No. 2018-0911. R.M. is a CIFAR Azrieli Global Scholar in the Gravity & the Extreme Universe Program, 2019 and an Alfred P. Sloan Fellow in Physics, 2019. B.M. is supported by NASA through the NASA Hubble Fellowship grant #HST-HF2-51412.001-A awarded by the Space Telescope Science Institute, which is operated by the Association of Universities for Research in Astronomy, Inc., for NASA, under contract NAS5-26555. The VLA observations presented here were obtained as part of programs VLA/17B-171, PI: Berger and VLA/19A-295, PI: Eftekhari. The VLA is operated by the National Radio Astronomy Observatory, a facility of the National Science Foundation operated under cooperative agreement by Associated Universities, Inc. This paper makes use of the following ALMA data: ADS/JAO.ALMA#2017.1.00280.S., ADS/JAO.ALMA#2019.1.01663.S. ALMA is a partnership of ESO (representing its member states), NSF (USA) and NINS (Japan), together with NRC (Canada), MOST and ASIAA (Taiwan), and KASI (Republic of Korea), in cooperation with the Republic of Chile. The Joint ALMA Observatory is operated by ESO, AUI/NRAO and NAOJ.

Software: Boxfit (van Eerten et al. 2012), CASA (McMullin et al. 2007), CLOUDY (Ferland et al. 2013), MOSFIT (Guillochon et al. 2018), pwkit (Williams et al. 2017).

Appendix
Brief Description of Sources in Our Sample

A.1. SN1999as

SN1999as ($z \approx 0.127$) was discovered on 1999 February 18 by the Supernova Cosmology Project (Knop et al. 1999). From Knop et al. (1999), the peak time is MJD 51242. Given its similarity to SN2007bi, we assume a 62 day rest-frame rise time, corresponding to an explosion date of MJD 51172. Spectroscopic data are given in Hatano et al. (2001). Observations of the host galaxy are given in Leloudas et al. (2015), Angus et al. (2016), and Schulze et al. (2018).

A.2. SN2005ap

SN2005ap ($z \approx 0.28$) was discovered on 2005 March 3 in images taken with the Robotic Optical Transient Search Experiment Telescope (ROTSE-IIIb; Akerlof et al. 2003) as part of the Texas Supernova Search (Quimby 2006). SN2005ap exhibited a 1–3 week rise to peak and a relatively rapid decay (Quimby et al. 2007). We assume a rest-frame rise time of 12 days and a peak time of MJD 53439 (Quimby et al. 2011b), corresponding to an explosion date of 53424. Radio and optical observations of the host are presented in Schulze et al. (2018). Additional host galaxy observations are given in Lunnan et al. (2014).

A.3. SN2006oz

SN2006oz ($z \approx 0.38$) was discovered on 2006 October 20 by the Sloan Digital Sky Survey II. We assume an explosion date of MJD 54025. Light curves and spectroscopy are given in Leloudas et al. (2012). Host galaxy observations are given in Lunnan et al. (2014), Leloudas et al. (2015), and Schulze et al. (2018).

A.4. SN2007bi

SN2007bi ($z \approx 0.13$) was discovered on 2007 April 6 by the Nearby Supernova Factory (Nugent 2007). The SN exhibited a slow rise time of 77 days with a peak time of MJD 54152, corresponding to an explosion date of MJD 54075 (Gal-Yam et al. 2009). Host galaxy observations are given in Lunnan et al. (2014) and Schulze et al. (2018). The relatively slow decay time and the large inferred mass of radioactive ^{56}Ni have been used to argue for a pair-instability supernova explosion (Gal-Yam et al. 2009), although Nicholl et al. (2013) have shown that the event properties are well matched to a magnetar central engine with a modest ejecta mass.

A.5. SN2009jh

SN2009jh (=PTF09cwl=CSS090802:144910+292510; $z \approx 0.35$) was first discovered in the Catalina Sky Survey on 2009 August 2 (Drake et al. 2009) and independently during commissioning of the PTF system (Quimby et al. 2011b). From Quimby et al. (2011b), the peak time is MJD 55081 and the rest-frame rise time is ~50 days, corresponding to an explosion date of 55014. Light curves and spectroscopy are given in De Cia et al. (2018) and Quimby et al. (2018). Observations of the host galaxy are presented in Leloudas et al. (2015), Angus et al. (2016), Perley et al. (2016), and Schulze et al. (2018). Extensive X-ray observations with Swift-XRT spanning $\delta t = 48$–1961 days reveal no X-ray source at the location of the SN (Levan et al. 2013; Margutti et al. 2018).

A.6. PTF09cnd

PTF09cnd ($z \approx 0.26$) was first detected on 2009 July 13 by the Palomar Transient Factory with the 1.2 m Samuel Oschin Telescope during commissioning of the PTF system (Quimby et al. 2011b). From Inserra et al. (2013), the peak time is MJD 55069.145 and the rest-frame rise time is ~50 days. Thus the explosion date is MJD 55006. Spectra for PTF09cnd are given in Quimby et al. (2018). Observations and properties of the

host galaxy are presented in Neill et al. (2011), Leloudas et al. (2015), and Perley et al. (2016). A previous search for FRBs from this event was conducted in Hilmarsson et al. (2020). X-ray nondetections place limits on the unabsorbed fluxes between 10^{-13}–10^{-15} erg cm^{-2} s^{-1} (Levan et al. 2013; Margutti et al. 2018).

A.7. SN2010kd

SN2010kd ($z \approx 0.23$) was discovered on 2010 November 14 by ROTSE-IIIb (Akerlof et al. 2003). From Vinko et al. (2012), we assume a peak time of MJD 55554 and a rest-frame rise time of 50 days, corresponding to an explosion date of MJD 55499. Host galaxy observations are given in Leloudas et al. (2015) and Schulze et al. (2018). X-ray observations of the source span $\delta t \sim 120$–1964 days post-explosion (rest frame) and correspond to limits on the unabsorbed X-ray flux of 10^{-13}–10^{15} erg cm^{-2} s^{-1} (Levan et al. 2013; Margutti et al. 2018).

A.8. SN2010gx

SN2010gx (=PTF10cwr=CSS100313:112547-084941; $z \approx 0.23$) was discovered by the Catalina Real-time Transient Survey on 2010 March 13 (Mahabal et al. 2010). From Inserra et al. (2013), the peak time is MJD 55279, and the rest-frame rise time is ∼23 days; the explosion date is therefore MJD 55251. Light curves and spectra are given in Quimby et al. (2011b) and Inserra et al. (2013). Host galaxy observations are given in Chen et al. (2013), Lunnan et al. (2014), Leloudas et al. (2015), Perley et al. (2016), and Schulze et al. (2018). A previous search for FRBs from this event was conducted in Hilmarsson et al. (2020). Swift-XRT observations spanning $\delta t = 19$–659 days reveal no X-ray source at the location of the SN (Levan et al. 2013; Margutti et al. 2018).

A.9. SN2011ke

SN2011ke (=PTF11dij=CSS110406:135058+261642=PS1-11xk; $z \approx 0.14$) was discovered by the Catalina Real-time Transient Survey on 2011 April 4 (Drake et al. 2011) and independently by the Palomar Transient Factory on 2011 March 30 (Quimby et al. 2011c). A non-detection of the event one day prior to the 2011 March 30 detection constrains the explosion date to MJD 55650.65 (Inserra et al. 2013). Host galaxy observations are given in Lunnan et al. (2014), Leloudas et al. (2015), Perley et al. (2016), and Schulze et al. (2018). Swift-XRT observations span $\delta t \sim 40 - 1604$ days post-explosion and reveal no X-ray source at the transient position (Levan et al. 2013; Margutti et al. 2018).

A.10. SN2011kf

SN2011kf (=CSS111230:143658+163057; $z \approx 0.25$) was discovered on 2011 December 30 by the Catalina Real-time Transient Survey (Drake et al. 2012). Additional spectra were obtained by Prieto et al. (2012). From Inserra et al. (2013), the inferred explosion date is MJD 55920.65. Host galaxy observations are given in Lunnan et al. (2014), Leloudas et al. (2015), and Schulze et al. (2018).

A.11. SN2011kg

SN2011kg (=PTF11rks; $z \approx 0.19$) was discovered on 2011 December 21 by the Palomar Transient Factory (Quimby et al. 2011a). From Inserra et al. (2013), the explosion date is MJD 55912.1. Host galaxy photometry and spectroscopy are given in Lunnan et al. (2014) and Perley et al. (2016). Swift-XRT observations reveal no X-ray source at the position of the SN over the time period $\delta t \sim 11$–25 days (Levan et al. 2013; Margutti et al. 2018).

A.12. SN2012il

SN2012il (=PS1-12fo=CSS120121:094613+195028; $z \approx 0.18$) was discovered by the Pan-STARRS1 3Pi Faint Galaxy Supernova Survey on 2012 January 19 (Smartt et al. 2012a) and independently by the Catalina Real-time Transient Survey on 2012 January 21 (Drake et al. 2012). From Inserra et al. (2013), the explosion date is MJD 55918.56. Observations of the host galaxy are presented in Lunnan et al. (2014), Leloudas et al. (2015), and Schulze et al. (2018). No X-ray emission is detected at the location of the source down to $\sim 10^{-16}$ erg s^{-1} cm^{-2} (Levan et al. 2013; Margutti et al. 2018).

A.13. PTF12dam

PTF12dam ($z \approx 0.11$) was discovered by the Palomar Transient Factory on 2012 April 10 (Quimby et al. 2012), and is among the subset of slowly evolving SLSNe (Nicholl et al. 2013; Inserra et al. 2017; Vreeswijk et al. 2017; Quimby et al. 2018). From Nicholl et al. (2013), the peak date is MJD 56088, and the rest-frame rise time is ∼60 days; the inferred explosion date is thus MJD 56022. Extensive studies of the host galaxy are presented in the literature (Lunnan et al. 2014; Chen et al. 2015; Leloudas et al. 2015; Thone et al. 2015; Perley et al. 2016; Hatsukade et al. 2018). The source is not detected in Swift-XRT observations over the timescale $\delta t \sim 43 - 900$ days down to a limiting flux of $F_X \sim 5 \times 10^{-14}$ erg s^{-1} cm^{-2} (Margutti et al. 2018). Chandra X-ray observations over the range $\delta t \sim 60$–68 days reveal an X-ray source with an unabsorbed flux $F_x = (7.3 \pm 2.9) \times 10^{-16}$ erg s^{-1} cm^{-2} (0.3–10 keV; Margutti et al. 2018). A previous search for FRBs from this event was conducted in Hilmarsson et al. (2020).

A.14. LSQ12dlf

LSQ12dlf ($z \approx 0.26$) was discovered by the La Silla-Quest survey (LSQ; Baltay et al. 2013) on 2010 July 10 and subsequently classified as an SLSN by the Public ESO Spectroscopic Survey of Transient Objects (PESSTO; Smartt et al. 2012b). From Nicholl et al. (2014), the peak time is MJD 56,149 and the rest-frame rise time is approximately ∼24 days. The inferred explosion date is therefore MJD 56119. A previous search for FRBs from this event was conducted in Hilmarsson et al. (2020). Host galaxy observations are given in Schulze et al. (2018).

A.15. SSS120810

SSS120810 ($z \approx 0.16$) was discovered on 2012 August 10 by the Catalina Real-time Transient Survey and subsequently classified as an SLSN by PESSTO (Wright et al. 2012). From Nicholl et al. (2014), the peak time is MJD 56146. Assuming a rest-frame rise time of 26 days, the explosion date is MJD 56116. Observations of the host galaxy are given in Leloudas et al. (2015) and Schulze et al. (2018).

A.16. SN2013dg

SN2013dg (=CSS130530:131841-070443=MLS130517:131841-07044; $z \approx 0.27$) was discovered on 2013 May 17 by the Mount Lemmon Survey and independently by the Catalina Sky Survey on 2018 May 30 (Drake et al. 2013). From Nicholl et al. (2014), the peak time is MJD 56449 and the rest-frame rise time is approximately 24 days. The inferred explosion date is therefore MJD 56419. Host galaxy observations are given in Schulze et al. (2018).

A.17. LSQ14bdq

LSQ14bdq ($z \approx 0.35$) was discovered by the LSQ on 2014 April 5 and subsequently classified by PESSTO (Benitez et al. 2014). The light curve exhibits an initial peak lasting ~15 days followed by a slower rise to maximum light (Nicholl et al. 2015). Nondetections prior to the initial peak constrain the explosion date to MJD 56721. Host galaxy observations are given in Schulze et al. (2018).

A.18. LSQ14mo

LSQ14mo ($z \approx 0.25$) was discovered by the LSQ on 2014 January 30 and subsequently classified by PESSTO as an SLSN on 2014 January 31 (Leloudas et al. 2014). From Leloudas et al. (2015), the peak time is MJD 56699. Assuming a rest-frame rise time of 50 days, the inferred explosion date is MJD 56636. Host galaxy observations are given in Chen et al. (2017) and Schulze et al. (2018). Swift-XRT observations over the timescale $\delta t \sim 52$–774 days rest-frame post-explosion do not show evidence for X-ray emission (Margutti et al. 2018).

A.19. LSQ14an

LSQ14an ($z \approx 0.16$) was discovered by the LSQ on 2014 January 3 and classified as an SLSN by PESSTO (Leget et al. 2014). The light curve indicates that LSQ14an is part of the class of slowly evolving SLSN (Inserra et al. 2017). From Jerkstrand et al. (2017), the peak time is MJD 56595. Assuming a rest-frame rise time of ~70 days, the inferred explosion date is MJD 56513. Host galaxy observations are given in Schulze et al. (2018). No X-ray emission is detected at the location of the source based on Swift-XRT observations spanning $\delta t \sim 64$–234 days rest-frame post-explosion (Margutti et al. 2018).

A.20. LSQ14fxj

LSQ14fxj ($z \approx 0.36$) was discovered by the LSQ on 2014 October 12 and classified as an SLSN I by PESSTO (Smith et al. 2014). From Smith et al. (2014), on MJD 56940, the source was 4−5 weeks post-maximum light. We assume a rest-frame rise time of 50 days, as in Margutti et al. (2018). The explosion date is MJD 56882. Host galaxy observations are given in Schulze et al. (2018). Swift-XRT observations of the source span $\delta t \sim 64$–234 days rest-frame post-explosion, and do not reveal any X-ray emission at the location of the source (Inserra et al. 2017; Margutti et al. 2018).

A.21. CSS140925

CSS140925 ($z \approx 0.46$) was discovered on 2014 September 25 by the Catalina Sky Survey and classified by PESSTO (Campbell 2014). From the CRTS catalog (http://nesssi.cacr.caltech.edu/catalina/AllSN.html), the explosion date is MJD 56900. No X-ray emission is detected at the SN location over the timescale $\delta t \sim 29$–186 days rest-frame post-explosion (Margutti et al. 2018). Host galaxy observations are given in Schulze et al. (2018).

A.22. SN2015bn

SN2015bn (=PS15ae=CSS141223-113342+004332=MLS150211-113342 +004333; $z \approx 0.11$) was initially discovered by the Catalina Sky Survey on 2014 December 23 (Drake et al. 2009). It was subsequently discovered by the Mount Lemmon Survey on 2015 February 11 and the Pan-STARRS Survey for Transients on 2015 February 15 (Huber et al. 2015). Host galaxy observations are presented in Schulze et al. (2018). Spectroscopy and UV to near-IR photometry spanning −50 to +250 days from optical maximum revealed a slowly fading source with undulations in the light curve on a timescale of 30–50 days (Nicholl et al. 2016b). Late-time, nebular-phase observations show evidence for a central engine (Nicholl et al. 2016a; Jerkstrand et al. 2017). Radio emission is not detected at 320–335 days post-explosion (Nicholl et al. 2016b). X-ray observations correspond to upper limits on the unabsorbed flux in the range 10^{-14}–10^{-13} erg cm^{-2} s^{-1} (Margutti et al. 2018).

A.23. OGLE15sd

OGLE15sd ($z \approx 0.57$) was discovered on 2015 November 7 by the Optical Gravitational Lensing Experiment (OGLE; Wyrzykowski et al. 2015). From the OGLE-IV Transient Detection System, the explosion date is MJD 57295 (http://ogle.astrouw.edu.pl/ogle4/transients/transients.html). No X-ray emission is detected at the SN location over the timescale $\delta t \sim 34$–212 days rest-frame post-explosion (Margutti et al. 2018).

A.24. iPTF16bad

iPTF16bad ($z \approx 0.2467$) was discovered on 2016 May 31 by the Intermediate Palomar Transient Factory (iPTF; Yan et al. 2017). The event is among a small subset of SLSNe displaying Hα emission at late times. We constrain the explosion date to MJD 57513 by fitting the optical light curve to a magnetar model using the Modular Open-Source Fitter for Transients (`MOSFit`).

A.25. SN2016ard

SN2016ard (=PS16aqv=CSS160216:141045-100935; $z \approx 0.16$) was discovered on 2016 February 20 by the Pan-STARRS near-Earth object survey (Chambers et al. 2016) and classified by Chornock et al. (2016). From Blanchard et al. (2018), the peak time is MJD 57453 and the rest-frame rise time is 17 days, corresponding to an explosion date of MJD 57433.4. Swift-XRT observations span $\delta t \sim 53$–131 days rest-frame since explosion and do not show evidence for X-ray emission at the SN location (Margutti et al. 2018).

A.26. SN2016els

SN2016els (=AT2016els=PS16dnq; $z \approx 0.217$) was discovered on 2016 July 29 by PESSTO (Mattila et al. 2016). From the Open Supernova Catalog, the peak date is MJD 57604. We assume a 50 day rest-frame rise time for an explosion date of MJD 57543.

A.27. SN2017gci

SN2017gci (=AT2017gci=Gaia17cbp; $z \approx 0.09$) was discovered on 2017 August 12 by the Gaia Photometric Survey (Delgado et al. 2017) and subsequently classified as an SLSN by ePESSTO (Lyman et al. 2017). We constrain the explosion date to MJD 57939 by fitting the optical light curve to a magnetar model using `MOSFit`.

A.28. SN2017jan

SN2017jan (=AT2017jan=OGLE17jan; $z \approx 0.396$) was discovered on 2017 December 18 by OGLE (Wyrzykowski & Gromadzki 2017) and subsequently classified by ePESSTO (Angus et al. 2017). We constrain the explosion date to MJD 57986 by fitting the optical light curve to a magnetar model using `MOSFit`.

A.29. SN2018bsz

SN2018bsz (=ASASSN-18km=AT2018bsz=ATLAS18pny; $z \approx 0.0267$) was discovered on 2018 May 17 by the All Sky Automated Survey for SuperNovae (Brimacombe et al. 2018) and detected independently by the Asteroid Terrestrial-impact Last Alert System (ATLAS) on 2018 May 21. From Anderson et al. (2018), the explosion date is estimated as the mid-point between the last non-detection epoch and the discovery date and is given by MJD 58202.5. Properties of the host galaxy are also given in Anderson et al. (2018).

A.30. SN2018gft

SN2018gft (=AT2018gf=ZTF18abshezu=ATLAS18uymActions; $z \approx 0.23$) was discovered on 2018 September 2 by the Zwicky Transient Facility (ZTF; Fremling 2018a). We constrain the explosion date to MJD 58355 by fitting the optical light curve to a magnetar model using `MOSFit`.

A.31. SN2018ffj

SN2018ffj (=AT2018ffj=ATLAS18tec; $z \approx 0.234$) was discovered on 2018 August 7 by ATLAS (Tonry et al. 2018a) and classified as an SLSN by ePESSTO on 2018 August 19 (Kostrzewa-rutkowska et al. 2018). From the Open Supernova Catalog, the peak date is MJD 58337. We assume a 50 day rest-frame rise time, corresponding to an explosion date of MJD 58275.

A.32. SN2018ffs

SN2018ffs (=AT2018ffs=ATLAS18txu=ZTF18ablwafp; $z \approx 0.142$) was discovered on 2018 August 13 by ATLAS (Tonry et al. 2018a) and classified by ePESSTO on 2018 September 16 (Gromadzki et al. 2018). We constrain the explosion date to MJD 58324 by fitting the optical light curve to a magnetar model using `MOSFit`.

A.33. SN2018hti

SN2018hti (=AT2018hti=ATLAS18yff=MLS181110:034054+114637=Gaia19amt; $z \approx 0.063$) was discovered on 2018 November 2 by ATLAS (Tonry et al. 2018b) and classified by the Global Supernova Project (Burke et al. 2018). We constrain the explosion date to MJD 58415 by fitting the optical light curve to a magnetar model using `MOSFit`.

A.34. SN2018ibb

SN2018ibb (=AT2018ibb=ATLAS18unu=ZTF18acenqto=Gaia19cvo; $z \approx 0.16$) was discovered on 2018 September 10 by ATLAS (Tonry et al. 2018c) and subsequently classified by ZTF (Fremling et al. 2018). From the Open Supernova Catalog, the peak date is MJD 58465. We assume a 50 day rest-frame rise time, corresponding to an explosion date of MJD 58407.

A.35. SN2018jfo

SN2018jfo (=AT2018jfo=ZTF18achdidy=MLS181220:112339+255952; $z \approx 0.163$) was discovered on 2018 November 10 by ZTF (Fremling 2018b) and subsequently classified as an SLSN on 2019 January 5 (Fremling et al. 2019). We constrain the explosion date to MJD 58411 by fitting the optical light curve to a magnetar model using `MOSFit`.

A.36. SN2018lfe

SN2018lfe (=AT2018lfe=PS18cpp=ZTF18acqyvag; $z \approx 0.35$) was discovered on 2018 December 31 by the Pan-STARRS Survey for Transients (Chambers et al. 2019) and subsequently classified as an SLSN on 2019 February 6 (Gomez et al. 2019). We constrain the explosion date to MJD 58424 by fitting the optical light curve to a magnetar model using `MOSFit`.

A.37. GRB 020903

GRB 020903 (=XRF020903; $z \approx 0.251$) was discovered on 2002 September 3 by the Wide-Field X-Ray monitor and the Soft X-Ray Camera on the High Energy Transient Explorer-2 (HETE-II; Soderberg et al. 2004). Observations of the radio and optical afterglow are presented in Soderberg et al. (2004). Host galaxy observations are given in Michałowski et al. (2012) and Greiner et al. (2016).

A.38. GRB 030329

GRB 030329 ($z \approx 0.168$) was discovered by the HETE-II satellite 2003 March 29 (Vanderspek et al. 2003). Radio observations of the afterglow, which is observable to $\delta t \sim 5$ yr post-explosion, are presented in Mesler et al. (2012) and van der Horst et al. (2008). Optical and radio observations of the host galaxy are presented in Niino et al. (2017) and Michałowski et al. (2012), respectively.

A.39. GRB 050826

GRB 050826 ($z \approx 0.296$) was discovered on 2005 August 26 by the Swift Burst Alert Telescope (BAT; Mangano et al. 2005). The event is categorized as a sub-luminous, sub-energetic event (Mirabal et al. 2007). A previous search for FRBs from this event was conducted in Hilmarsson et al. (2020). Host galaxy observations are presented in Levesque et al. (2010) and Niino et al. (2017).

A.40. GRB 061021

GRB 061021 ($z \approx 0.3463$) was discovered by the Swift-BAT on 2006 October 21 (Moretti et al. 2006). The event is one of a small subset of GRBs that exhibit excess X-ray emission at early times, which has been attributed to thermal emission from the shock breakout of a supernova (Sparre & Starling 2012).

Optical and radio observations of the host galaxy are presented in Michałowski et al. (2012), Perley et al. (2015), and Greiner et al. (2016).

A.41. GRB 090417B

GRB 090417B ($z \approx 0.345$) was discovered on 2009 April 17 by the Swift-BAT (Sbarufatti et al. 2009). The burst is classified as a "dark" GRB, a small subset of events lacking optical afterglows. Optical and radio observations of the host galaxy are given in Perley & Perley (2013) and Perley et al. (2013), respectively.

A.42. GRB 111225A

GRB 112225A ($z \approx 0.297$) was discovered on 2011 December 25 by the Swift-BAT (Siegel et al. 2011). A previous search for FRBs from this event was conducted in Hilmarsson et al. (2020). Host galaxy observations are not reported in the literature for this event.

A.43. GRB 120422A

GRB 120422A ($z \approx 0.283$) was discovered and localized by the Swift-BAT on 2012 April 22 (Troja et al. 2012). The event is classified as a transition object between low- and high-luminosity GRBs (Schulze et al. 2014). Host galaxy observations are presented in Niino et al. (2017).

ORCID iDs

T. Eftekhari https://orcid.org/0000-0003-0307-9984
B. Margalit https://orcid.org/0000-0001-8405-2649
C. M. B. Omand https://orcid.org/0000-0002-9646-8710
E. Berger https://orcid.org/0000-0002-9392-9681
P. K. Blanchard https://orcid.org/0000-0003-0526-2248
P. Demorest https://orcid.org/0000-0002-6664-965X
B. D. Metzger https://orcid.org/0000-0002-4670-7509
K. Murase https://orcid.org/0000-0002-5358-5642
M. Nicholl https://orcid.org/0000-0002-2555-3192
V. A. Villar https://orcid.org/0000-0002-5814-4061
K. D. Alexander https://orcid.org/0000-0002-8297-2473
S. Chatterjee https://orcid.org/0000-0002-2878-1502
D. L. Coppejans https://orcid.org/0000-0001-5126-6237
J. M. Cordes https://orcid.org/0000-0002-4049-1882
S. Gomez https://orcid.org/0000-0001-6395-6702
G. Hosseinzadeh https://orcid.org/0000-0002-0832-2974
K. Kashiyama https://orcid.org/0000-0003-4299-8799
R. Margutti https://orcid.org/0000-0003-4768-7586

References

Akerlof, C. W., Kehoe, R. L., McKay, T. A., et al. 2003, PASP, 115, 132
Alexander, K. D., Laskar, T., Berger, E., et al. 2017a, ApJ, 848, 69
Alexander, K. D., Wieringa, M. H., Berger, E., Saxton, R. D., & Komossa, S. 2017b, ApJ, 837, 153
Anderson, J. P., Pessi, P. J., Dessart, L., et al. 2018, A&A, 620, A67
Angus, C. R., Jones, S., Angus, C. R., et al. 2017, TNSCR, 2017-1495, 1
Angus, C. R., Levan, A. J., Perley, D. A., et al. 2016, MNRAS, 458, 84
Baltay, C., Rabinowitz, D., Hadjiyska, E., et al. 2013, PASP, 125, 683
Bannister, K. W., Deller, A. T., Phillips, C., et al. 2019, Sci, 365, 565
Barniol Duran, R., & Giannios, D. 2015, MNRAS, 454, 1711
Bell, E. F. 2003, ApJ, 586, 794
Beloborodov, A. M. 2017, ApJL, 843, L26
Benitez, S., Polshaw, J., Inserra, C., et al. 2014, ATel, 6118, 1
Berger, E., Cowie, L. L., Kulkarni, S. R., et al. 2003, ApJ, 588, 99
Berger, E., Kulkarni, S. R., & Chevalier, R. A. 2002, ApJL, 577, L5
Berger, E., Kulkarni, S. R., & Frail, D. A. 2001, ApJ, 560, 652
Berger, E., Kulkarni, S. R., Pooley, G., et al. 2003, Natur, 426, 154
Berger, E., Zauderer, A., Pooley, G. G., et al. 2012, ApJ, 748, 36
Bhandari, S., Sadler, E. M., Prochaska, J. X., et al. 2020, ApJL, 895, L37
Blanchard, P. K., Berger, E., Nicholl, M., & Villar, V. A. 2020, ApJ, 897, 114
Blanchard, P. K., Nicholl, M., Berger, E., et al. 2018, ApJ, 865, 9
Bochenek, C. D., Ravi, V., Belov, K. V., et al. 2020, Natur, 587, 59
Bose, S., Dong, S., Pastorello, A., et al. 2018, ApJ, 853, 57
Bright, J., Mooley, K., Fender, R., et al. 2017, ATel, 10538, 1
Brimacombe, J., Castro, N., Clocchiatti, A., et al. 2018, ATel, 11660, 1
Bromberg, O., & Tchekhovskoy, A. 2016, MNRAS, 456, 1739
Brown, G. C., Levan, A. J., Stanway, E. R., et al. 2017, MNRAS, 472, 4469
Burke, J., Hiramatsu, D., Arcavi, I., et al. 2018, TNSCR, 2018-1719, 1
Campbell, H. 2014, ATel, 6523, 1
Cenko, S. B., Frail, D. A., Harrison, F. A., et al. 2010, ApJ, 711, 641
Cenko, S. B., Krimm, H. A., Horesh, A., et al. 2012, ApJ, 753, 77
Chambers, K. C., Huber, M. E., Flewelling, H., et al. 2016, TNSTR, 2016-175, 1
Chambers, K. C., Huber, M. E., Flewelling, H., et al. 2019, TNSTR, 2019-5, 1
Chandra, P., Cenko, S. B., Frail, D. A., et al. 2008, ApJ, 683, 924
Chandra, P., & Frail, D. A. 2012, ApJ, 746, 156
Chandra, P., Ofek, E. O., Frail, D. A., et al. 2009, ATel, 2241, 1
Chandra, P., Ofek, E. O., Frail, D. A., et al. 2010, ATel, 2367, 1
Chatterjee, S., Law, C. J., Wharton, R. S., et al. 2017, Natur, 541, 58
Chen, T. W., Nicholl, M., Smartt, S. J., et al. 2017, A&A, 602, A9
Chen, T.-W., Smartt, S. J., Bresolin, F., et al. 2013, ApJL, 763, L28
Chen, T. W., Smartt, S. J., Jerkstrand, A., et al. 2015, MNRAS, 452, 1567
Chevalier, R. A. 1982, ApJ, 258, 790
Chevalier, R. A. 1998, ApJ, 499, 810
Chevalier, R. A., & Irwin, C. M. 2011, ApJL, 729, L6
Chevalier, R. A., Li, Z.-Y., & Fransson, C. 2004, ApJ, 606, 369
Chomiuk, L., Chornock, R., Soderberg, A. M., et al. 2011, ApJ, 743, 114
Chomiuk, L., Soderberg, A., Margutti, R., et al. 2012, ATel, 3931, 1
Chornock, R., Bhirombhakdi, K., Katebi, R., et al. 2016, ATel, 8790, 1
Condon, J. J. 1992, ARA&A, 30, 575
Condon, J. J., Anderson, M. L., & Helou, G. 1991, ApJ, 376, 95
Coppejans, D. L., Margutti, R., Guidorzi, C., et al. 2018, ApJ, 856, 56
Coppejans, D. L., Margutti, R., Terreran, G., et al. 2020, ApJL, 895, L23
Cordes, J. M., & Chatterjee, S. 2019, ARA&A, 57, 417
Cordes, J. M., & McLaughlin, M. A. 2003, ApJ, 596, 1142
Cornwell, T. J., Golap, K., & Bhatnagar, S. 2008, ISTSP, 2, 647
Corsi, A., Gal-Yam, A., Kulkarni, S. R., et al. 2016, ApJ, 830, 42
Curran, P. A., Evans, P. A., de Pasquale, M., Page, M. J., & van der Horst, A. J. 2010, ApJL, 716, L135
De Cia, A., Gal-Yam, A., Rubin, A., et al. 2018, ApJ, 860, 100
Delgado, A., Harrison, D., Hodgkin, S., et al. 2017, TNSTR, 2017-873, 1
Drake, A. J., Djorgovski, S. G., Mahabal, A., et al. 2009, ApJ, 696, 870
Drake, A. J., Djorgovski, S. G., Mahabal, A., et al. 2013, CBET, 3560, 1
Drake, A. J., Djorgovski, S. G., Mahabal, A. A., et al. 2011, ATel, 3343, 1
Drake, A. J., Djorgovski, S. G., Mahabal, A. A., et al. 2012, ATel, 3873, 1
Eftekhari, T., Berger, E., Margalit, B., et al. 2019, ApJL, 876, L10
Eftekhari, T., Berger, E., Zauderer, B. A., Margutti, R., & Alexander, K. D. 2018, ApJ, 854, 86
Ferland, G. J., Porter, R. L., van Hoof, P. A. M., et al. 2013, RMxAA, 49, 137
Filho, M. E., Tabatabaei, F. S., Sánchez Almeida, J., Muñoz-Tuñón, C., & Elmegreen, B. G. 2019, MNRAS, 484, 543
Fremling, C. 2018a, TNSTR, 2018-1368, 1
Fremling, C. 2018b, TNSTR, 2018-2046, 1
Fremling, C., Dugas, A., & Sharma, Y. 2018, TNSCR, 2018-1877, 1
Fremling, C., Dugas, A., & Sharma, Y. 2019, TNSCR, 2019-32, 1
Gaensler, B. M., & Slane, P. O. 2006, ARA&A, 44, 17
Gal-Yam, A. 2012, Sci, 337, 927
Gal-Yam, A., Mazzali, P., Ofek, E. O., et al. 2009, Natur, 462, 624
Gomez, S., Blanchard, P., Hosseinzadeh, G., Berger, E., & Nicholl, M. 2019, ATel, 12478, 1
Gourdji, K., Michilli, D., Spitler, L. G., et al. 2019, ApJL, 877, L19
Greiner, J., Michałowski, M. J., Klose, S., et al. 2016, A&A, 593, A17
Gromadzki, M., Wevers, T., Lyman, J., & Yaron, O. 2018, TNSCR, 2018-1396, 1
Gruzinov, A. 2005, PhRvL, 94, 021101
Guillochon, J., Nicholl, M., Villar, V. A., et al. 2018, ApJS, 236, 6
Hatano, K., Maeda, K., Deng, J. S., et al. 2001, in ASP Conf. Ser. 251, New Century of X-ray Astronomy, ed. H. Inoue & H. Kuieda (San Francisco, CA: ASP), 244
Hatsukade, B., Tominaga, N., Hayashi, M., et al. 2018, ApJ, 857, 72
Heintz, K. E., Prochaska, J. X., Simha, S., et al. 2020, ApJ, 903, 152

Helou, G., Soifer, B. T., & Rowan-Robinson, M. 1985, ApJL, 298, L7
Hilmarsson, G. H., Spitler, L. G., Keane, E. F., et al. 2020, MNRAS, 493, 5170
Hindson, L., Kitchener, G., Brinks, E., et al. 2018, ApJS, 234, 29
Ho, A. Y. Q., Perley, D. A., Kulkarni, S. R., et al. 2020, ApJ, 895, 49
Ho, A. Y. Q., Phinney, E. S., Ravi, V., et al. 2019, ApJ, 871, 73
Huber, M., Chambers, K. C., Flewelling, H., et al. 2015, ATel, 7153, 1
Inserra, C., Nicholl, M., Chen, T. W., et al. 2017, MNRAS, 468, 4642
Inserra, C., Smartt, S. J., Jerkstrand, A., et al. 2013, ApJ, 770, 128
Irwin, J. A., Henriksen, R. N., Krause, M., et al. 2015, ApJ, 809, 172
Jerkstrand, A., Smartt, S. J., Inserra, C., et al. 2017, ApJ, 835, 13
Kasen, D., & Bildsten, L. 2010, ApJ, 717, 245
Kashiyama, K., & Murase, K. 2017, ApJL, 839, L3
Kashiyama, K., Murase, K., Bartos, I., Kiuchi, K., & Margutti, R. 2016, ApJ, 818, 94
Kasliwal, M. M., Cenko, S. B., Singer, L. P., et al. 2016, ApJL, 824, L24
Kathirgamaraju, A., Barniol Duran, R., & Giannios, D. 2016, MNRAS, 461, 1568
Knop, R., Aldering, G., Deustua, S., et al. 1999, IUAC, 7128, 1
Kostrzewa-rutkowska, Z., Callis, E., Fraser, M., & Yaron, O. 2018, TNSCR, 2018-1212, 1
Laskar, T., Alexander, K. D., Berger, E., et al. 2016, ApJ, 833, 88
Laskar, T., Berger, E., Margutti, R., et al. 2015, ApJ, 814, 1
Laskar, T., Berger, E., Zauderer, B. A., et al. 2013, ApJ, 776, 119
Law, C. J., Butler, B. J., Prochaska, J. X., et al. 2020, ApJ, 899, 161
Law, C. J., Gaensler, B. M., Metzger, B. D., Ofek, E. O., & Sironi, L. 2018, ApJL, 866, L22
Law, C. J., Omand, C. M. B., Kashiyama, K., et al. 2019, ApJ, 886, 24
Leget, P. F., Le Guillou, L., Fleury, M., et al. 2014, ATel, 5718, 1
Leloudas, G., Chatzopoulos, E., Dilday, B., et al. 2012, A&A, 541, A129
Leloudas, G., Ergon, M., Taddia, F., et al. 2014, ATel, 5839, 1
Leloudas, G., Schulze, S., Krühler, T., et al. 2015, MNRAS, 449, 917
Levan, A. J., Read, A. M., Metzger, B. D., Wheatley, P. J., & Tanvir, N. R. 2013, ApJ, 771, 136
Levesque, E. M., Kewley, L. J., Berger, E., & Zahid, H. J. 2010, AJ, 140, 1557
Lunnan, R., Chornock, R., Berger, E., et al. 2014, ApJ, 787, 138
Lunnan, R., Chornock, R., Berger, E., et al. 2018, ApJ, 852, 81
Lyman, J., Homan, D., Magee, M., & Yaron, O. 2017, TNSCR, 2017-881, 1
MacFadyen, A. I., & Woosley, S. E. 1999, ApJ, 524, 262
MacFadyen, A. I., Woosley, S. E., & Heger, A. 2001, ApJ, 550, 410
Macquart, J. P., Prochaska, J. X., McQuinn, M., et al. 2020, Natur, 581, 391
Mahabal, A. A., Drake, A. J., Djorgovski, S. G., et al. 2010, ATel, 2490, 1
Mangano, V., Barbier, L., Blustin, A., et al. 2005, GCN, 3884, 1
Marcote, B., Nimmo, K., Hessels, J. W. T., et al. 2020, Natur, 577, 190
Marcote, B., Paragi, Z., Hessels, J. W. T., et al. 2017, ApJL, 834, L8
Margalit, B., Beniamini, P., Sridhar, N., & Metzger, B. D. 2020, ApJL, 899, L27
Margalit, B., Berger, E., & Metzger, B. D. 2019, ApJ, 886, 110
Margalit, B., & Metzger, B. D. 2018, ApJL, 868, L4
Margalit, B., Metzger, B. D., Berger, E., et al. 2018a, MNRAS, 481, 2407
Margalit, B., Metzger, B. D., Thompson, T. A., Nicholl, M., & Sukhbold, T. 2018b, MNRAS, 475, 2659
Margalit, B., & Piran, T. 2020, MNRAS, 495, 4981
Margutti, R., Chornock, R., Metzger, B. D., et al. 2018, ApJ, 864, 45
Margutti, R., Metzger, B. D., Chornock, R., et al. 2019, ApJ, 872, 18
Margutti, R., Milisavljevic, D., Soderberg, A. M., et al. 2014, ApJ, 797, 107
Mattila, S., Fraser, M., Reynolds, T., et al. 2016, ATel, 9308, 1
Mattila, S., Pérez-Torres, M., Efstathiou, A., et al. 2018, Sci, 361, 482
Mazzali, P. A., Foley, R. J., Deng, J., et al. 2007a, ApJ, 661, 892
Mazzali, P. A., Kawabata, K. S., Maeda, K., et al. 2007b, ApJ, 670, 592
Mazzali, P. A., McFadyen, A. I., Woosley, S. E., Pian, E., & Tanaka, M. 2014, MNRAS, 443, 67
Mazzali, P. A., Nomoto, K., Patat, F., & Maeda, K. 2001, ApJ, 559, 1047
McMullin, J. P., Waters, B., Schiebel, D., Young, W., & Golap, K. 2007, in ASP Conf. Ser. 376, Astronomical Data Analysis Software and Systems XVI, ed. R. A. Shaw, F. Hill, & D. J. Bell (San Francisco, CA: ASP), 127
Mesler, R. A., Pihlström, Y. M., Taylor, G. B., & Granot, J. 2012, ApJ, 759, 4
Metzger, B. D., Berger, E., & Margalit, B. 2017, ApJ, 841, 14
Metzger, B. D., Giannios, D., Thompson, T. A., Bucciantini, N., & Quataert, E. 2011, MNRAS, 413, 2031
Michałowski, M. J., Gentile, G., Hjorth, J., et al. 2015, A&A, 582, A78
Michałowski, M. J., Kamble, A., Hjorth, J., et al. 2012, ApJ, 755, 85
Michilli, D., Seymour, A., Hessels, J. W. T., et al. 2018, Natur, 553, 182
Mirabal, N., Halpern, J. P., & O'Brien, P. T. 2007, ApJL, 661, L127
Mizuta, A., & Ioka, K. 2013, ApJ, 777, 162
Modjaz, M., Kewley, L., Kirshner, R. P., et al. 2008, AJ, 135, 1136
Mondal, S., Bera, A., Chandra, P., & Das, B. 2020, MNRAS, 498, 3863
Moretti, A., Barthelmy, S. D., Gehrels, N., et al. 2006, GCN, 5743, 1
Murase, K., Kashiyama, K., Kiuchi, K., & Bartos, I. 2015, ApJ, 805, 82
Murase, K., Kashiyama, K., & Mészáros, P. 2016, MNRAS, 461, 1498
Murase, K., Omand, C., Nagai, H., et al. 2020, MNRAS, submitted
Murphy, E. J., Condon, J. J., Schinnerer, E., et al. 2011, ApJ, 737, 67
Neill, J. D., Sullivan, M., Gal-Yam, A., et al. 2011, ApJ, 727, 15
Nicholl, M., Berger, E., Blanchard, P. K., Gomez, S., & Chornock, R. 2019, ApJ, 871, 102
Nicholl, M., Berger, E., Margutti, R., et al. 2016a, ApJL, 828, L18
Nicholl, M., Berger, E., Margutti, R., et al. 2017a, ApJL, 845, L8
Nicholl, M., Berger, E., Margutti, R., et al. 2017b, ApJL, 835, L8
Nicholl, M., Berger, E., Smartt, S. J., et al. 2016b, ApJ, 826, 39
Nicholl, M., Blanchard, P. K., Berger, E., et al. 2018, ApJL, 866, L24
Nicholl, M., Guillochon, J., & Berger, E. 2017c, ApJ, 850, 55
Nicholl, M., Smartt, S. J., Jerkstrand, A., et al. 2013, Natur, 502, 346
Nicholl, M., Smartt, S. J., Jerkstrand, A., et al. 2014, MNRAS, 444, 2096
Nicholl, M., Smartt, S. J., Jerkstrand, A., et al. 2015, ApJL, 807, L18
Nicholl, M., Williams, P. K. G., Berger, E., et al. 2017d, ApJ, 843, 84
Niino, Y., Aoki, K., Hashimoto, T., et al. 2017, PASJ, 69, 27
Nugent, P. E. 2007, CBET, 929, 1
Omand, C. M. B., Kashiyama, K., & Murase, K. 2018, MNRAS, 474, 573
Palliyaguru, N. T., Corsi, A., Frail, D. A., et al. 2019, ApJ, 872, 201
Panaitescu, A., & Kumar, P. 2002, ApJ, 571, 779
Perley, D. A., Levan, A. J., Tanvir, N. R., et al. 2013, ApJ, 778, 128
Perley, D. A., & Perley, R. A. 2013, ApJ, 778, 172
Perley, D. A., Perley, R. A., Hjorth, J., et al. 2015, ApJ, 801, 102
Perley, D. A., Quimby, R. M., Yan, L., et al. 2016, ApJ, 830, 13
Peters, C., van der Horst, A. J., Chomiuk, L., et al. 2019, ApJ, 872, 28
Piro, A. L. 2016, ApJL, 824, L32
Planck Collaboration, Adam, R., Ade, P. A. R., et al. 2016, A&A, 594, A1
Prieto, J. L., Drake, A. J., Mahabal, A. A., et al. 2012, ATel, 3883, 1
Prochaska, J. X., Macquart, J.-P., McQuinn, M., et al. 2019, Sci, 366, 231
Quimby, R. M. 2006, PhD thesis (Univ. Texas)
Quimby, R. M., Aldering, G., Wheeler, J. C., et al. 2007, ApJL, 668, L99
Quimby, R. M., Arcavi, I., Sternberg, A., et al. 2012, ATel, 4121
Quimby, R. M., De Cia, A., Gal-Yam, A., et al. 2018, ApJ, 855, 2
Quimby, R. M., Gal-Yam, A., Arcavi, I., et al. 2011a, ATel, 3841, 1
Quimby, R. M., Kulkarni, S. R., Kasliwal, M. M., et al. 2011b, Natur, 474, 487
Quimby, R. M., Sternberg, A., & Matheson, T. 2011c, ATel, 3344, 1
Ransom, S. M. 2001, PhD thesis (Harvard Univ.)
Ravi, V., Catha, M., D'Addario, L., et al. 2019, Natur, 572, 352
Rhoads, J. E. 1997, ApJL, 487, L1
Roychowdhury, S., & Chengalur, J. N. 2012, MNRAS, 423, L127
Sari, R., Piran, T., & Halpern, J. P. 1999, ApJL, 519, L17
Sault, R. J., & Wieringa, M. H. 1994, A&AS, 108, 585
Saxton, R. D., Read, A. M., Komossa, S., et al. 2017, A&A, 598, A29
Sbarufatti, B., Barthelmy, S. D., Baumgartner, W. H., et al. 2009, GCN, 9135, 1
Scholz, P. & Chime/Frb Collaboration 2020, ATel, 13681, 1
Schulze, S., Krühler, T., Leloudas, G., et al. 2018, MNRAS, 473, 1258
Schulze, S., Malesani, D., Cucchiara, A., et al. 2014, A&A, 566, A102
Siegel, M. H., Baumgartner, W. H., Chester, M. M., et al. 2011, GCN, 12720, 1
Smartt, S. J., Inserra, C., Fraser, M., et al. 2012b, ATel, 4299, 1
Smartt, S. J., Wright, D., Valenti, S., et al. 2012a, ATel, 3918, 1
Smith, M., Firth, R., Dimitriadis, G., et al. 2014, ATel, 6739, 1
Smolčić, V., Novak, M., Bondi, M., et al. 2017, A&A, 602, A1
Soderberg, A. M., Chakraborti, S., Pignata, G., et al. 2010, Natur, 463, 513
Soderberg, A. M., Kulkarni, S. R., Berger, E., et al. 2004, ApJ, 606, 994
Soderberg, A. M., Kulkarni, S. R., Berger, E., et al. 2005, ApJ, 621, 908
Soderberg, A. M., Margutti, R., Zauderer, B. A., et al. 2012, ApJ, 752, 78
Soderberg, A. M., Nakar, E., Berger, E., & Kulkarni, S. R. 2006, ApJ, 638, 930
Sparre, M., & Starling, R. L. C. 2012, MNRAS, 427, 2965
Spitkovsky, A. 2006, ApJL, 648, L51
Spitler, L. G., Cordes, J. M., Hessels, J. W. T., et al. 2014, ApJ, 790, 101
Spitler, L. G., Scholz, P., Hessels, J. W. T., et al. 2016, Natur, 531, 202
Stratta, G., Gendre, B., Atteia, J. L., et al. 2013, ApJ, 779, 66
Tanaka, S. J., & Takahara, F. 2010, ApJ, 715, 1248
Tanaka, S. J., & Takahara, F. 2013, MNRAS, 429, 2945
Tchekhovskoy, A., Spitkovsky, A., & Li, J. G. 2013, MNRAS, 435, L1
Tendulkar, S. P., Bassa, C. G., Cordes, J. M., et al. 2017, ApJL, 834, L7
Thompson, T. A., Chang, P., & Quataert, E. 2004, ApJ, 611, 380
Thone, C. C., de Ugarte Postigo, A., Garcia-Benito, R., et al. 2015, MNRAS, 451, L65
Tonry, J., Denneau, L., Heinze, A., et al. 2018b, TNSTR, 2018-1680, 1
Tonry, J., Denneau, L., Heinze, A., et al. 2018c, TNSTR, 2018-1722, 1
Tonry, J., Stalder, B., Denneau, L., et al. 2018a, TNSTR, 2018-1210, 1

Troja, E., D'Elia, V., Guidorzi, C., et al. 2012, GCN, 13243, 1
van der Horst, A. J., Kamble, A., Resmi, L., et al. 2008, A&A, 480, 35
van Eerten, H., van der Horst, A., & MacFadyen, A. 2012, ApJ, 749, 44
Vanderspek, R., Crew, G., Doty, J., et al. 2003, GCN, 1997, 1
Vinko, J., Zheng, W., Pandey, S. B., et al. 2012, AAS Meeting, 219, 436.04
Vreeswijk, P. M., Leloudas, G., Gal-Yam, A., et al. 2017, ApJ, 835, 58
Wang, X.-G., Zhang, B., Liang, E.-W., et al. 2015, ApJS, 219, 9
Wellons, S., Soderberg, A. M., & Chevalier, R. A. 2012, ApJ, 752, 17
Williams, P. K. G., Clavel, M., Newton, E., & Ryzhkov, D. 2017, pwkit: Astronomical utilities in Python, ascl:1704.001
Woosley, S. E. 2010, ApJL, 719, L204
Woosley, S. E., Langer, N., & Weaver, T. A. 1995, ApJ, 448, 315
Wright, D., Cellier-Holzem, F., Inserra, C., et al. 2012, ATel, 4313, 1
Wyrzykowski, L., & Gromadzki, M. 2017, TNSTR, 2017-1442, 1
Wyrzykowski, L., Kostrzewa-Rutkowska, Z., Klencki, J., et al. 2015, ATel, 8485, 1
Yan, L., Lunnan, R., Perley, D. A., et al. 2017, ApJ, 848, 6
Yan, L., Quimby, R., Ofek, E., et al. 2015, ApJ, 814, 108
Yost, S. A., Harrison, F. A., Sari, R., & Frail, D. A. 2003, ApJ, 597, 459
Young, D. R., Smartt, S. J., Valenti, S., et al. 2010, A&A, 512, A70
Zauderer, B. A., Berger, E., Margutti, R., et al. 2013, ApJ, 767, 152
Zauderer, B. A., Berger, E., Soderberg, A. M., et al. 2011, Natur, 476, 425